REVISITING THE SCATTERING REGIME MAP BASED ON TRANSPORT SCATTERING COEFFICIENT

by

Aristo Taufiq

S.T., Mechanical Engineering, Universitas Gadjah Mada, 2018

Submitted to the Institute for Graduate Studies in
Science and Engineering in partial fulfillment of
the requirements for the degree of
Master of Science

Graduate Program in Mechanical Engineering

Boğaziçi University

2023

ACKNOWLEDGEMENTS

I would like to express my deepest gratitude to two of my supervisors, Prof. Hakan Ertürk and Refet Ali Yalçın, Ph.D., for their unwavering guidance, invaluable insights, and unending patience throughout the entire research process. Thank you for intoducing me to the radiation transfer field, it has been a hard journey, but with your truly inspiring mentorship, we have accomplished this work which hopefully will impact the field.

I would like to also mention my family (mother, brother, and sister), for their unconditional love, encouragement, and continuous support and for allowing me to leave our country to pursue my dream. My friends, internationals, Turkish and my countrymen alike, and classmates throughout my study, who have been a source of motivation, camaraderie, and laughter during both the highs and lows of this journey. Your presence has made the academic experience all the more enjoyable.

I would like to express my deepest gratitude to YTB for the scholarship and for affording me the opportunity to study at Boğaziçi University. The successful completion of this thesis and my studies was made possible through their invaluable financial support.

Lastly, our lifespan as a human is short, so I would like to apologize for everything I did wrong to whomever that I would not cross-path again. But I pray to God Almighty that He would bestow upon us the strength to keep working towards good deeds and warn each other of the bad. And we would walk the path of the righteous. And we would hold on to the strong bond, so we would see each other again under the paradise light, together forever in the day after.

ABSTRACT

REVISITING THE SCATTERING REGIME MAP BASED ON TRANSPORT SCATTERING COEFFICIENT

Radiative transfer in media consisting of randomly dispersed particles is commonly found in various scientific and engineering applications. The norm for analyzing such systems is to use the independent scattering assumption, where the radiative characteristics of the system are derived from the superposition of the individual particles' radiative characteristics. One criterion for the validity of this assumption is that the particles are sparsely distributed. If this is not the case, estimation of properties for dependent scattering necessitates a more rigorous analysis. Historically, researchers have established regime maps that are used to identify if the independent scattering assumption is valid. However, recent experiments in the literature have shown that the well-established regime map may have shortcomings and predicts certain cases to be within the validity of the independent scattering assumption, although they are not. In this paper, a new regime map is sought considering the effect of particle refractive index. The study is established through numerical simulations using the static structure factor that accounts for the dependent scattering. The approach is validated with an experimentally verified method based on the T-matrix method, considering only the incoherent component of the scattered electric field, which represents the scattering of electromagnetic waves propagating through a dense medium. Coherent and incoherent coefficients were overlooked in recent studies, resulting in erroneous interpretations of the location of the demarcation line and the effect of the refractive index. To rectify this, the present study uses the transport scattering coefficient as a single intrinsic characteristic to define the transition between independent and dependent scattering. The transport scattering coefficient has been proven to correlate well with reflectance, unlike the scattering coefficient and the asymmetry parameter.

ÖZET

ULAŞTIRMA DAĞILIM KATSAYISINA DAYALI DAĞILIM REJİM HARİTASININ GÖZDEN GEÇİRİLMESİ

Rastgele dağılmış parçacıklardan oluşan ortamlarda ışın geçişi, çeşitli bilimsel ve mühendislik uygulamalarında yaygın olarak bulunmaktadır. Bu tür sistemleri analiz etmek için genellikle bağımsız saçılma varsayımı kullanılır; burada sistemlerin ışın özellikleri, bireysel parçacıkların ışın özelliklerinin üst üste bindirilmesiyle elde edilir. Bu varsayımın geçerliliği için bir kriter, parçacıkların seyrek bir şekilde dağıtılmış olmasıdır. Eğer durum böyle değilse, bağımlı saçılma için özellik tahmini daha kesin bir analiz gerektirir. Tarih boyunca, araştırmacılar, bağımsız saçılma varsayımının geçerli olup olmadığını belirlemek için kullanılan rejim haritaları oluşturmuşlardır. Ancak, literatürdeki son deneyler, iyi belirlenmiş rejim haritasının eksikliklere sahip olabileceğini ve belirli durumların bağımsız saçılma varsayımının geçerliliği içinde olduğunu tahmin ettiğini göstermiştir, ancak aslında değildir. Bu çalışmada, parçacık yansıma indisinin etkisi göz önünde bulundurularak yeni bir rejim haritası aranmaktadır. Çalışma, bağımlı saçılmayı hesaba katan statik yapı faktörünü kullanarak sayısal simülasyonlarla kurulmuştur. Yakın geçmişteki çalışmalarda koherent ve koher olmayan katsayılar göz ardı edilmiştir, bu da demarkasyon çizgisinin konumunun ve yansıma indisinin etkisinin yanlış yorumlanmasına yol açmıştır. Bu çalışma, bağımsız ve bağımlı saçılma arasındaki geçişi tanımlamak için tek bir özgün karakteristik olarak taşıma saçılma katsayısını kullanır. Çünkü taşıma saçılma katsayısının, saçılma katsayısı ve asimetrilik parametresinin aksine yansımayla iyi bir şekilde ilişkili olduğu kanıtlanmıştır. Bu çalışma, sıkı bir ortamda ilerleyen elektromanyetik dalgaların saçılmasını temsil eden koher olmayan bileşen dikkate alınarak deneysel olarak doğrulanmış bir yönteme dayanan T-matris yöntemi ile doğrulanmıştır.

TABLE OF CONTENTS

LIST OF FIGURES

LIST OF TABLES

LIST OF SYMBOLS

a_n	Lorenz-Mie coefficient
B	Magnetic induction
b_n	Lorenz-Mie coefficient
C_{abs}	Absorption cross-section
C_{ext}	Extinction cross-section
C_{sca}	Scattering cross-section
D	Diameter of the scattering particle
$\mathbf{D}$	Electric displacement field
$\mathbf{E}$	Electric field
$\mathbf{E}^{\text{inc}}$	Incident scattered electric field
$\mathbf{E}^{\text{sca}}$	Total scattered electric field
$\mathbf{E}^{\text{sca,c}}$	Coherent scattered electric field
$\mathbf{E}^{\text{sca,ic}}$	Incoherent scattered electric field
$\mathbf{E}_{\text{part}}$	Electric field scattered by single particle
E_g	Deviation calculated using asymmetry parameter
E_R	Deviation calculated using reflectance
E_σ	Deviation calculated using scattering coefficient
$E_{\sigma'}$	Deviation calculated using transport scattering coefficient
$f(r^*)$	Radial/pair distribution
f_v	Volume fraction
g	Asymmetry parameter
g_{dep}	Asymmetry parameter considering dependent scattering
g_{ind}	Asymmetry parameter assuming independent scattering
$\mathbf{H}$	Magnetic field
$I_{\text{s,part}}$	Intensity field scattered by a single particle
$I_{\text{s,tot}}$	Intensity field scattered as total by an ensemble
I_λ	Spectral intensity field
$I_{\lambda,i}$	Spectral intensity field at incident

$I_{\lambda,r}$	Spectral intensity field for reflectance
$\mathbf{J}$	Current density
l_s	Scattering mean free path
l_s'	Transport scattering mean free path
m	Relative refractive index
n_{m}	Refractive index of the host
n_{p}	Refractive index of the particle
$\mathbf{P}$	Polarization density
$P(r^*)$	Number of particle counted
R_{e}	Radius of ensemble
R_{nh}	Normal-hemispherical reflectance
$R_{\mathrm{nh,dep}}$	Normal-hemispherical reflectance, dependent scattering
$R_{\mathrm{nh,ind}}$	Normal-hemispherical reflectance, independent scattering
$\boldsymbol{r}$	Location vector
r^*	Distance from central scatterer
s	Distance traversed by radiation
T	T-matrix, total
T^{c}	Coherent T-matrix
T^{ic}	Incoherent T-matrix
T_{nh}	Normal-hemispherical transmittance
V_{e}	Volume of the emsemble
V_{p}	Volume of the scattering particle
β^{ic}	Incoherent extinction coefficient
ϵ	Electric permittivity
θ	Polar scattering angle
θ_r	Polar scattering angle for reflectance
κ_λ	Spectral absorption coefficient
λ	wavelength
μ	Magnetic permeability or $\cos\theta$
ρ	Number density

$\sigma_{\mathrm{s,dep}}$	Scattering coefficient, dependent scattering
$\sigma_{\mathrm{s,ind}}$	Scattering coefficient, independent scattering
$\sigma_{s,\lambda}$	Spectral scattering coefficient
σ'_{s}	Transport scattering coefficient
$\sigma'_{\mathrm{s,dep}}$	Transport scattering coefficient, dependent scattering
$\sigma'_{\mathrm{s,ind}}$	Transport scattering coefficient, independent scattering
Φ_λ	Spectral phase function
φ_r	Azimuth angle for reflectance
χ	Size parameter
Ω	Solid angle
ω^{ic}	Incoherent albedo

LIST OF ACRONYMS/ABBREVIATIONS

EM	Electromagnetic
ISA	Independent Scattering Assumption
IVEGen	Incoherent Volume Element Generator
MAC	Multiparticle Averaging Clearance
MCM	Monte Carlo Method
PyPI	Python Package Index
RAM	Random Access Memory
RTE	Radiative Transfer Equation
R^2T^2	Radiative Transfer with Reciprocal Transaction
SD	Standard deviation
SSF	Static Structure Factor

1. INTRODUCTION

1.1. Motivation

The propagation of electromagnetic waves (EM) within a medium consisting of sphere like scatterers is observed in applications such as combustion [1], paints and coatings [2], atmospheric science [3], oceanology [4], photonics [5], and biomedical research and treatment [6]. Though the EM wave propagation is governed by Maxwell's equations, it is not possible to solve them for a domain whose size is much larger than the incident wavelength due to the excess computational resources the solution requires. An alternative approach is to formulate propagation through relatively thick media relying on the radiative transfer equation (RTE), as it can also account for absorption, emission, and scattering [7]. The RTE solves the local radiative intensity field by considering the radiative characteristics of the medium such as the scattering phase function, scattering coefficient, and absorption coefficient. Thus, it is necessary to obtain the radiative characteristics of the medium prior to solving the RTE.

Although phenomenological RTE has been well established for almost a century, its derivation from macroscopic Maxwell equations was quite recent [8]. The derivation assumes: (i) The scattering particles are distanced apart from each other with respect to the incident wavelength; (ii) the observation point is far from the scattering object; (iii) the motion of the particles is independent of each other; (iv) no correlation exists between the particles' physical state and their positions; (v) scattering particles are many in number; (vi) the system is ergodic, meaning that the average characteristics of the system can be represented by taking the average of states from a sufficiently large random sample. These assumptions indicate that the interaction of the incident wave with a single particle in the medium is not affected by the presence of other particles. This is referred to as independent scattering approximation (ISA). If ISA is valid for systems consisting of spherical scatterers, Lorenz-Mie theory, which is the

analytical solution of Maxwell's equations for a single sphere [9], can be used to define the radiative characteristics of the domain relying on the superposition principle.

Dependent scattering prevails if ISA is not valid [10]. For media consisting of randomly distributed particles at high volume fraction, the interparticle distance is small relative to the incident wavelength [1], [11, 12]. For such cases, the scattered waves from different particles interfere with each other, affecting the overall intensity field, and relying on the superposition of the scattering cross section of individual particles to calculate the scattering coefficient of the medium is no longer valid. Dependent scattering manifests itself by an observed decrease of the scattering efficiency with increasing volume fraction for randomly dispersed dielectric particles [12, 13]. Additionally, it can be observed when the measured reflectance and/or transmittance values differ from those estimated based on ISA [11], [14]. As more rigorous analysis is required to capture the effects of dependent scattering, researchers have been interested in identifying the applicability limits of ISA since the 1980s. Using available data of measured reflectance/tranmittances, they seek to establish a regime map that can be used to identify the validity of ISA for a system with a known volume fraction and particle size parameter [1, 12, 14].

1.2. Literature Survey

1.2.1. Physical Interpretation of Independent and Dependent Scattering

The study of radiative transfer can be described as the study of EM waves interactions between different bodies. EM waves emanating from a body are formed due to energy emission, which are caused by a combination of electronic and molecular oscillations, transition in the emitting material, and lattice vibration [15]. This emitted energy from an object will then radiate to other objects. One example of the interaction involves how EM waves may partially lose their energy to a receiving body. This phenomenon is called absorption. Another phenomenon called scattering describes how the energy of the EM waves propagates, including any redirection of the radiative

energy that was not absorbed. Reflection, refraction, diffraction, and transmission are all included in the term "scattering".

In the topic of radiative transfer, the topic of interest is to gain an understanding of the energy that is transferred between the surfaces that are involved [7]. These surfaces may be separated between a medium such as a vacuum or a medium consisting of randomly distributed particles. A medium would be considered to be "participating" if it has a role in altering the radiative energy that is crossing along a path. In scattering, this alteration only includes redirection of the energy, which in turn may cause a decrease or increase of the overall energy along a given path of the propagation.

The nature of which scattering is happening in a particulate medium differs from one case to another depending on the size, shape, position of the constituent particles, refractive index of both the particles' and matrix's, and wavelength of the propagating EM waves. Suppose that all of these parameters can be determined prior to an analysis, then the quantity of energy that is propagating can theoretically be obtained for a defined incident intensity. Considering scattering in a case where [16]: (1) the particles are located far apart from each other (each particle is in the "far-field" region of each other's), (2) the observation point is in the far-field region of the collection of particles that is considered as the scattering medium, (3) the position and state of each particle are statistically independent with each other, and (4) the distribution of the particles is completely random and statistically uniform. For a medium that satisfies (1), (3), and (4), the constituent particles that form the medium can be called "independent scatterers" [16]. The difference between radiative energy after following a given path from the initial state on the incident side would follow proportionally to the number of scatterers incident to the radiation. Each individual scatterer would see other scatterers as point scatterers, and the contribution of scattering from each particle can be added together, independently of each other's contribution, following the superposition principle. Thus, the term "independent scattering" refers to such an occasion. The approach of independent scattering allowed for the total radiative property of a particle cloud to be obtained by summing the radiative property of the

individual particles that make up the cloud [13], [17]. The procedures involved in the calculation of the radiative property considering independent scattering will be the topic of discussion in Section 2.3.

In contrast to the previous case, consider the case where the radiative energy is propagating inside a medium that is densely packed with scattering particles. This case will directly violate condition (1) that was previously discussed, as the particles would clearly be in close proximity with each other. Furthermore, it can be proven that densely packed particles are not totally uncorrelated, that is, the distribution is not statistically uniform (will be discussed in Section 2.4.2), which would violate condition (4). In such a case, the surrounding particles affect the internal radiation field of a particle (near-field effect). Additionally, the radiative energy outgoing from the individual scatterer may interfere destructively or constructively with what is outgoing from another particle (far-field effect) [15]. The consequences of both near-field and far-field effects is that the medium's property that described the scattering cannot be obtained simply through adding individual contribution of each particle. This case is regarded as "dependent scattering". The consequences to the existence of the dependent scattering effects on the formulation of the solution in radiative transfer are given in Section 2.4.

1.2.2. Regime Map

The first proper scattering regime map that identifies independent and dependent scattering zones was proposed by Brewster and Tien [1]. The experimental data used were from their experimental works and those of Hottel *et al.* [11], which served as the basis for drawing a line of clearance-to-wavelength ratio, $c/\lambda = 0.3$, to delineate between the two regimes. The definition of c/λ itself was taken from the rhombohedral correlation for random particle spacing, $c/\lambda = (0.905/f_{\mathrm{v}}^{1/3} - 1)\chi/\pi$. Here, f_{v} is the particle volume fraction and $\chi = \pi D/\lambda$ is the size parameter with D being the diameter of the particles. Further investigation of the regime map was carried out and published in a two-part study by the same group, including theoretical evaluation [18]

and further experiments [14]. The theoretical study employed the Rayleigh-Debye scattering approximation combined with two different form factors to account for the dependent scattering effects; the gas model and the packed-sphere model. Considering 5% deviation from the ISA based estimation of scattering efficiency, they redefined the demarcation line as $c/\lambda = 0.5$. Furthermore, two additional limits were also identified to define the region: (i) of $f_v < 0.6\%$ since it is deduced that independent scattering always prevails for anything below this volume fraction; (ii) of $\chi > 9.5$, since no dependent scattering effect was observed above this size parameter. The study by Drolen *et al.* [12] then verified this finding, but kept the $c/\lambda = 0.5$ line to the high size parameter. This series of studies has become well-regarded in the community, even though there are other studies suggesting different criteria for the transition to the dependent scattering regime [17], [19–21]. Despite the different proposed criteria, the trend of setting the dependent scattering based on 5% deviation was taken to be standard in several studies that follow [22–24]. Both experimental measurements and numerical studies come with uncertainties, and the 5% deviation provides a reasonable transition between the two regimes while still being relatively conservative.

1.2.3. Recent Developments in Transition Criteria

Lee [22] extended the early regime map by establishing it for a medium consisting of fibrous material. The extinction efficiency of the medium can be obtained by solving the Maxwell's equations for EM waves that are incident normal to a medium consisting of infinitely long fibrous material. The ratio of extinction efficiency calculated considering the dependent scattering effect to the one calculated using ISA is used as a parameter to find the demarcation line between the dependent and independent scattering regime. When 5% deviation from ISA is taken at $m = 1.196$ (the values follow previous publications [1], [12], [14], [18]), the demarcation line produced became close to what had been proposed in [12]. It was also noted that at $\chi \leq 0.1$ the demarcation line is vertical at a constant f_v of 0.6% similar to the early regime map.

Another approach was taken by Ivezić and Mengüç [17], where they take an absorbing particle based on soot. Data based on the result of calculation of bisphere models performed using Discrete Dipole Approximation (DDA) was used to determine the minimum interparticle distance to consider dependent scattering effect. Their result shows that independent scattering can be applied safely for the cases of $\chi > 2$ and $c \geq 2.4/\chi$. For the case where $\chi \leq 2$ and $c < 2$, dependent scattering will prevail. Depending on the case, the radiative property can be approximated using either agglomerate model or effective sphere [25].

The relatively recent derivation of RTE directly from Maxwell's equations by Mishchenko [8] was based on the assumption that the position and state of particles are statistically independent of each other, an assumption within ISA. The experiments carried out by Mishchenko *et al.* [26], measuring the reflectance of a particulate media, suggest that RTE with ISA is reliable for volumetric packing densities up to 2%, but caution is advised for densities around 5%, and for 10%, where RTE with ISA is not reliable. Furthermore, in a statement, they mentioned that the limitation of RTE can be extended using a phenomenological patch by incorporating the Static Structure Factor (SSF). The suggested phenomenological patch was studied further in [27–29] and has been verified by Yalçın *et al.* [30] in a recent study.

More recently, Galy *et al.* [23] reviewed studies on dependent scattering and listed the critical criteria proposed by various authors. They also conducted a study motivated by how the proposed criteria in the literature for the demarcation of the two regimes were expressed by different parameters, formulated from a limited range of data, and in disagreement with each other. Their study was performed by using DDA for the case of bisphere, and also disordered and ordered suspensions and aggregates with up to 8 particles. The size parameter, inter-particle distance, and refractive index were also varied. They looked into the scattering cross section and the asymmetry parameter computed using DDA and then compared it with the corresponding values calculated using ISA. A more recent study by Aoyu *et al.* [24] criticized the the studies related to the 40-year-old regime map for their use of rhombohedral lattice-ordered

distribution when defining the inter-particle distance, neglecting the near-field effect, and use of only optically soft material. They proposed a method to obtain the value of c/λ for randomly distributed particles instead of relying on the rhombohedral lattice structure. Their study using the T-matrix method considered spherical particle ensembles with varying refractive indices, which goes beyond optically soft materials, and included absorbing particles. They considered using scattering cross section ratio (defined as ratio of cross sections calculated considering the effects of dependent scattering to those calculated based on ISA) as parameter, which was similar to other studies [22,23]. An increase in scattering cross section ratio is observed in these studies with introduction of dependent scattering effects for dielectric particles with $\chi < 2$. However, these findings contradict those presented by Drolen and Tien [13], where the scattering cross section ratio decreases as f_{v} increases. Lastly, in a recent study, Zhai *et al.* studied scattering from ensembles of particles with absorbing and non-absorbing host media using the T-matrix method. They proposed a criteria of $c/\lambda \geq 4.8$ and $c/\lambda \geq 2.52$, respectively for the two cases. While Drolen and Tien [13] rely on experimental data to support their results, the other studies [22–24], [31], rely on numerical analysis.

1.3. Objective

There are various shortcomings in the recent studies that investigate the scattering regime map solely based on EM theory [22–24], [31]. First, they focus on a limited domain, considering a limited number of f_{v} values and vary χ or choose a limited number of χ values and vary f_{v}. The approach is questionable as proposing a criteria that distinguishes independent and dependent scattering should not be viable after only investigating a restricted amount of points and regions on the map. Second, they were unable to observe the threshold of the dependent scattering at the low volume fraction which was determined to be $f_{\mathrm{v}} = 0.6\%$ as discovered by previous studies [14], [18] and supported with experiments [12]. Third, they consider finite-sized systems with EM waves incident to a cloud of particles from free-space which is not a representative case of wave propagation in an infinitely large dense medium. This approach results in an

overestimation of the scattering due to the existence of coherent scattering occurring at free-space - particulate medium boundary, which is not observed during EM wave propagation inside an infinitely large medium. Recent studies [22–24], [31], that seek new criteria for the transition between independent and dependent scattering were found to overlook the coherent scattering phenomenon at the boundary, thus, their study was plagued with the overestimation of the scattering. This explains the contradictory behavior in their result with that of by Drolen *et al.* [12] whereby they found an increase in scattering with the introduction of dependent scattering effects. It also presumed that their method produces error when asymmetry parameter is sought.

A remedy for solving RTE in dense media was previously proposed in the form of a framework referred to as Radiative Transfer with Reciprocal Transactions (R^2T^2) [32]. This method solves RTE with Monte Carlo method (MCM) by calculating the scattering characteristics of the medium from particle ensembles (using the T-matrix method) instead of a single particle (the Lorenz-Mie theory). This framework encompasses a particular methodology to deduct the influence of coherent reflection at the boundary of the scattering ensemble [33]. The means of deducting the coherent scattering effects for a system of spherical scatterers has been manifested in a open source code called Incoherent Volume Element Generator (IVEGen) [34], which will be discussed in Section 2.4.1.

Figure 1.1 shows the regime map from [1], [12] with the experimental data on which the map was based on [1], [11, 12], [14], also including a recent experiment by Mishchenko *et al.* [26] that motivates this study. The recent experimental study by Mishchenko *et al.* [26] showed that the accuracy of well-known regime map in [12] (as shown in Figure 1.1) is questionable. Other recent studies that revisited the regime map relying on analysis based on direct solution of Maxwell's equations investigated it in certain limited regions and proposed alternative c/λ demarcation lines accordingly [22–24], [31]. Furthermore, they overlooked coherent scattering leading to erroneous outcomes. In this study, we investigate the scattering regime map using Lorenz-Mie theory and SSF throughout the entirety of the map in detail. One

major difference between the experimental and theoretical studies so far is the evaluation metric. While experimental studies relied on measured and estimated reflectance/transmittance values, the theoretical studies relying on EM theory consider scattering cross sections/efficiencies/coefficients and/or asymmetry parameter as an evaluation metric. In this study we will also identify a proper evaluation metric for establishing a regime map. Once the evaluation metric is identified, the regime map at different particle refractive indices are investigated, identifying the effect of refractive index mismatch between medium and particle on the transition between regimes so that the refractive index dependent demarcation line can explain the discrepancy between the early scattering regime map [12, 13] and more recent experimental data [26].

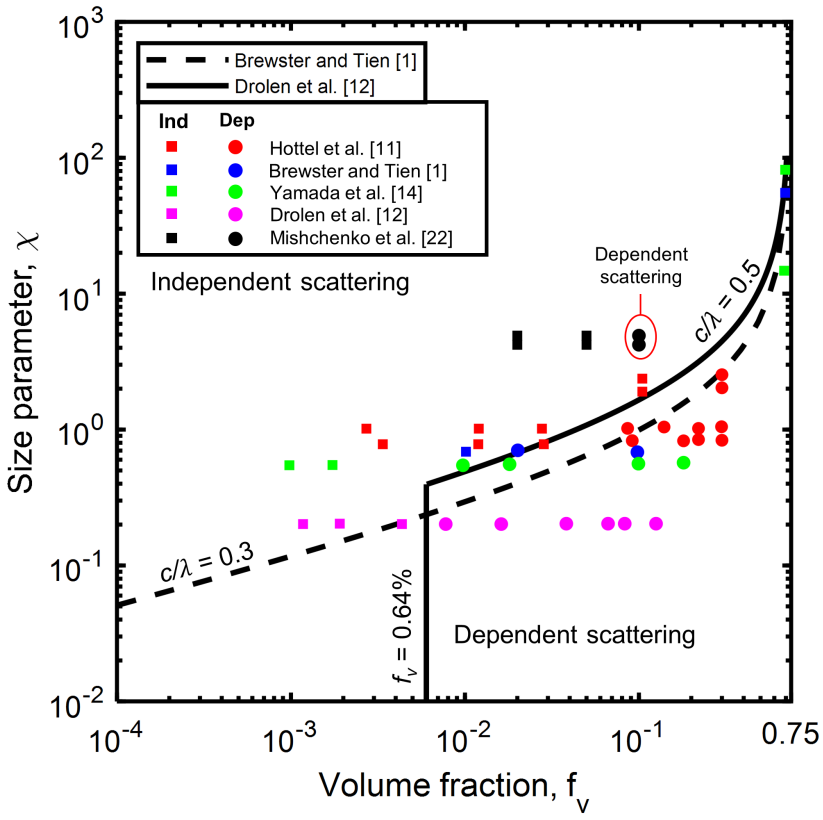

Figure 1.1. Scattering regime map and critical criteria proposed by different authors with experimental data to support some of their works. It is worth to note that the experimental work of Mishchenko [26], circled in red, does not agree with the previously proposed regime maps.

2. LIGHT SCATTERING IN SPHERICAL RANDOM MEDIUM

2.1. Maxwell's Equations

The fundemental of EM waves propagation is governed by the Maxwell's equations. The set of equations that correspond to Maxwell's equation, in its most general form, can be written as [7]

$$\nabla \cdot \mathbf{D} = \rho_e, \tag{2.1}$$

$$\nabla \cdot \mathbf{B} = 0, \tag{2.2}$$

$$\nabla \times \mathbf{E} = -\frac{\partial \mathbf{B}}{\partial t}, \tag{2.3}$$

$$\nabla \times \mathbf{H} = \mathbf{J} + \frac{\partial \mathbf{D}}{\partial t}, \tag{2.4}$$

where the vector field $\mathbf{E}$, $\mathbf{H}$, $\mathbf{D}$, $\mathbf{B}$, $\mathbf{J}$, and ρ_e are the electric field, magnetic field, electric displacement field, magnetic induction, current density, and free charge density, respectively. Constitutive relation is used to relate between some of the variables,

$$\mathbf{D} = \epsilon \mathbf{E} + \mathbf{P}, \tag{2.5}$$

$$\mathbf{B} = \mu \mathbf{H}, \tag{2.6}$$

where $\mathbf{P}$, ϵ, μ are the polarization density, electric permittivity, and magnetic permeability, respectively. To explain, consider an electric field which in turn create a displacement field due to how a slight separation between the nuclei, which is positively charged, and electron, which is negatively charged, is created (Equation 2.5). Equation 2.1 describes the distribution of the displacement field in relation to how the charges are distributed within a volume. The magnetic induction, $\mathbf{B}$ is linearly related to the magnetic field, $\mathbf{H}$, and the distribution is given by Equation 2.2. The value "0" in the right-hand-side of the equation suggest that there is no free magnetic sink/source term. Both Equation 2.1 and 2.2 explains phenomena regarding electrostatics. The Faraday's law of Equation 2.3 explains that time changing magnetic field induces electric field within a close loop. The Ampere's law of Equation 2.4 explains that time varying electric field induces magnetic field. Thus, it is clear that time varying electric field causes time varying magnetic field, which is the basis of EM waves propagation.

Describing light scattering problem directly by Maxwell's equations, without using approximations, undoubtedly will provide more insight to the behaviour of EM waves as how it is in nature. As light is inherently EM waves, the phenomenon such as interference, diffraction, and dispersion can be observed from the result of solving them. Other sub-wavelength phenomena such as plasmonics and near-field effects are also given by the direct solution of Maxwell's equations. However, for a complex problem with a macroscopic length scale, the directly solving Maxwell's equations may not be feasible to perform. The solution to this is by applying several assumptions to the case, which then can be use to manipulate the Maxwell's equations to derive RTE and provide approximation for the light scattering problems. The detail of the derivation is given in [8].

Relatively small cases of light scattering problems can be solved by finding the direct solution to the Maxwell's equations, and the methods themselves have been used in the study of dependent scattering [22–24], [31]. In this study, the direct solution of randomly distributed particle within spherical media is used as validation to justify the SSF. Thus, it is befitting to discuss the direct solution of the Maxwell's equation but only in the context of randomly distributed spherical media, which is of interest in this study. The discussion is presented in Section 2.4.1 as a part of chapter of calculation which considers dependent scattering effects.

2.2. Radiative Transfer Theory

Radiative transfer in a scattering, absorbing, and emitting medium can be described using the radiative transfer equation (RTE), which can be derived from the macroscopic Maxwell's equations under certain assumptions [8]. The RTE in terms of spectral intensity, I_λ, can be written as [7]

$$\frac{dI_\lambda(\boldsymbol{r},\Omega)}{ds} = -\kappa_\lambda I_\lambda(\boldsymbol{r},\Omega) - \sigma_{\mathrm{s},\lambda} I_\lambda(\boldsymbol{r},\Omega) + \frac{\sigma_{\mathrm{s},\lambda}}{4\pi}\int_{4\pi} I_\lambda(\boldsymbol{r},\Omega')\Phi_\lambda(\Omega',\Omega)d\Omega', \qquad (2.7)$$

where Ω is the solid angle and the infinitesimal value of it is defined as $d\Omega = \sin\theta d\varphi d\theta$, related to the polar angle, θ, and the azimuth angle φ. In the in-scattering term (third

term in the right hand side), the incident solid angle is described by Ω'. The RTE describes how the spectral intensity, $I_\lambda(\boldsymbol{r}, \Omega)$ at the location $\boldsymbol{r}$ at a particular direction changes as a field value. The subscript λ reflects the wavelength dependence of the quantity. The values κ_λ and $\sigma_{\mathrm{s},\lambda}$ are the absorption and scattering coefficients, respectively, while $\Phi_\lambda(\Omega', \Omega)$ is the scattering phase function that describes the distribution of the scattered intensity. Solving the RTE requires prior knowledge of the quantity of κ_λ, $\sigma_{\mathrm{s},\lambda}$, and $\Phi_\lambda(\Omega', \Omega)$, which are the radiative properties of a medium. In the framework of ISA, these values can be easily derived for a system of spherical scatterers simply from the Lorenz-Mie theory.

The RTE can be solved to calculate the normal-hemispherical reflectance in a case of scattering by a plane-parallel slab with a thickness of L formulated as [7]

$$R_{\mathrm{nh}} = \frac{\displaystyle\int_0^{2\pi}\int_0^{\pi/2} I_{\lambda,r}\left(L, \theta_r, \varphi_r\right)\cos\theta_r \sin\theta_r d\theta_r d\varphi_r}{I_{\lambda,i}\left(\theta_i = 0\right)}. \tag{2.8}$$

The subscript r suggests that the corresponding values are related to reflected direction, where reflected polar and azimuthal angles θ_r φ_r are defined with respect to the outward normal of the front surface of the slab (the side of incoming radiation). The denominator is for the normalization where the $I_{\lambda,i}$ is the incident intensity that is normally incident onto the slab. In the case where the scatterers and host medium (also referred to as matrix) are dielectric materials, i.e., absorption can be neglected, the energy balance of the system becomes $T_{\mathrm{nh}} + R_{\mathrm{nh}} = 1$, where T_{nh} is the normal-hemispherical transmittance.

While the scattering coefficient shows how strong the medium is scattering, its directional tendency of the scattering can be identified through the asymmetry parameter, g, that is defined based on the scattering phase function. Considering scattering by spherical particles, the phase function is independent of azimuthal angle and it is only a function of the polar angle, $\Phi_\lambda = \Phi_\lambda(\theta)$. With this assumption, the asymmetry

parameter represents the mean cosine of the scattering angle, and can be defined as

$$g = \langle \mu \rangle = \frac{1}{2} \int_{-1}^{1} \Phi_\lambda(\mu) \mu d\mu, \tag{2.9}$$

where $\mu = \cos(\theta)$. Based on this definition, g varies from -1 for the case of fully backscattering to 1 for the case of fully forward-scattering medium.

2.2.1. Radiative Transfer with Monte Carlo Method

The Monte Carlo method is a general term used to simulate a system relying on statistical sampling. The behaviour of the system is represented by events of which the probability of each event is independent of each others. In context of radiative transfer, the MCM is done by generating photon bundles which carries radiative energy. Photon's "life" are then evaluated considering physical events such as scattering and absorption. Whether or not the physical event takes part depends on a generated random number based on probability density functions which is derived from the nature of the events themselves. The sampling must be done over a number large enough to produce statistically accurate result.

The MCM for the solution of RTE is carried out by an open source code available in Python Package Index (PyPI) and Github [35]. This code has been used before in previous studies [36] and it uses collision-based MCM [37] algorithm. The plane-parallel medium is considered and boundary reflections are neglected. Exact scattering phase function is used instead of an approximation such as Henyey-Greenstein phase function.

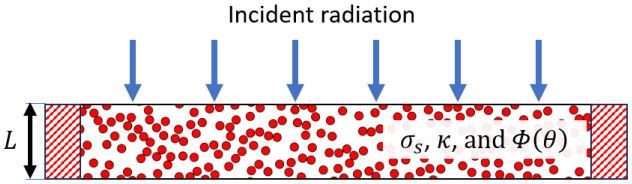

Figure 2.1. The problem of radiation incident to a plane parallel medium which is simulated by the MCM. Boundary reflection is neglected.

2.2.2. Transport Scattering Coefficient

The solution of RTE with the MCM in can be computationally expensive as the photon bundles required to obtain an accurate result can be high, especially in the case of optically thick media and forward scattering particles. When a photon propagates within a medium, it will be scattered after it travels a certain length. The mean value of the statistically sampled length corresponding to this is called "mean scattering path-length", l_s, and the reciprocal of this is the scattering coefficient, $\sigma_s = 1/l_s$ [38]. When scattering occurs, the direction to which the photons will be redirected is defined by $\Phi(\theta)$ and for most cases, scattering occurs anisotropically, meaning that the probability of the redirection of photons is not uniform for all angles. Using knowledge of l_s and $\Phi(\theta)$, MCM simulation can be performed and an accurate result can be obtained, given that enough photon bundles are simulated. In practice, the scattering pathlength scale can be relatively small, effectively allowing multitudes of scattering events to happen in the process, adding to the computational overhead. Additionally, the computation of the exact phase function, which is inherently anisotropic, adds to the complexity of the problem.

One approach to simplify the problem is to use the transport approximation [39], which involves introducing a simple form of phase function comprising an isotropic contribution combined with a forward scattering peak, formulated as

$$\Phi(\mu) = 1 - g + 2g\delta(1 - \mu). \tag{2.10}$$

The use of the phase function in 2.10 allows the RTE to be rewritten to a simpler form, whereby the scattering now is considered isotropic, i.e., [39, 40]

$$\frac{dI_\lambda(\boldsymbol{r}, \Omega)}{ds} = -\kappa_\lambda I_\lambda(\boldsymbol{r}, \Omega) - \sigma'_{\mathrm{s},\lambda} I_\lambda(\boldsymbol{r}, \Omega) + \frac{\sigma'_{\mathrm{s},\lambda}}{4\pi} \int_{4\pi} I_\lambda(\boldsymbol{r}, \Omega) d\Omega, \tag{2.11}$$

where $\sigma'_s = \sigma_s(1 - g)$ is called the transport scattering coefficient. Equation 2.11 is a simpler form of RTE given in Equation 2.7, when the σ'_s and the approximate phase function (Equation 2.10) is used, instead of σ_s and an exact scattering phase function. With the introduction of σ'_s, a new length scale defined as $l'_s = 1/\sigma'_s$ is introduced, known as the "transport mean free path" [38, 39]. This new length scale describes the

typical distance a photon travels before its direction is randomized. Consider the case shown in Figure 2.2 which involves a case where the scattering is mostly forward in direction ($0 < g < 1$). It is apparent that $\sigma'_{\mathrm{s}} < \sigma_{\mathrm{s}}$ and therefore $l'_s > l_s$. A higher length scale use in simulation will reduce the simulated scattering event within the medium and thus reducing the computational overhead.

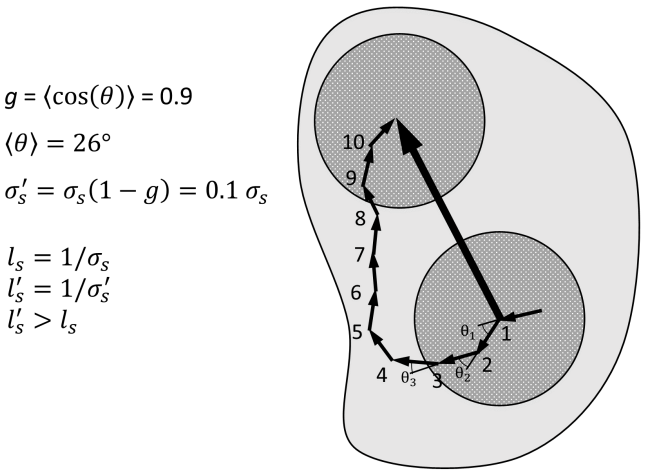

Figure 2.2. An illustration of the reduced path length when transport scattering coefficient is considered. The small arrow indicates the pathlength formed considering the exact anisotropic phase function, whereas the large arrow indicates the pathlength formed assuming simplified phase function.

It is worth emphasizing that the current study does not assume isotropic scattering approximation while solving RTE and uses the anisotropic scattering phase function as shown in Equation 2.7. For dielectric particles in a non-absorbing medium, the intensity field in anisotropic RTE (Equation 2.7) depends on both σ_{s} and $\Phi_\lambda(\theta)$, whereas in Equation 2.11, intensity only depends on σ'_{s}. Observing the effect of a single parameter on intensity field is more convenient for the purpose of the study. Therefore, the transport scattering coefficient is also used as an evaluation metric to locate the demarcation line between independent and dependent scattering regimes.

2.3. Independent Scattering

A case of sparsely distributed particles can be assumed to scatter independently. This section presents a discussion of how ISA is implemented for the case of spherical random media. The implementation for both monodisperse system and polydisperse system is discussed.

2.3.1. Lorenz-Mie Theory

Solving the Maxwell's equation for the case of single particle is the premise of the Lorenz-Mie theory [9]. The solution tells the scattering and absorption behaviour of a single spherical particle. It is important to note the importance of the solution of a single particle: the radiative characteristics of a medium can be derived from single particle solution. The Lorenz-Mie solution is exact, and the solution applies to spherical particles of any size.

Considering the relative refractive index of the dielectric scatters, $m = n_{\mathrm{p}}/n_{\mathrm{m}}$, the Lorenz-Mie coefficient can be described as

$$a_n = \frac{m\psi_n(m\chi)\psi_n'(\chi) - \psi_n(\chi)\psi_n'(m\chi)}{m\psi_n(m\chi)\xi'(\chi) - \xi_n(\chi)\psi_n'(m\chi)}, \tag{2.12}$$

$$b_n = \frac{\psi_n(m\chi)\psi_n'(\chi) - m\psi_n(\chi)\psi_n'(m\chi)}{\psi_n(m\chi)\xi'(\chi) - m\xi_n(\chi)\psi_n'(m\chi)}, \tag{2.13}$$

where the psi_n and xi_n is the Riccati-Bessel functions. The extinction, scattering, and absorption cross-section are defined as

$$C_{\mathrm{ext,LM}} = \frac{\pi D^2}{2\chi^2}\sum_{n=1}^{\infty}(2n+1)\mathrm{Re}(a_n + b_n), \tag{2.14}$$

$$C_{\mathrm{sca,LM}} = \frac{\pi D^2}{2\chi^2}\sum_{n=1}^{\infty}(2n+1)(|a_n|^2 + |b_n|^2), \tag{2.15}$$

$$C_{\mathrm{abs,LM}} = C_{\mathrm{ext,LM}} - C_{\mathrm{sca,LM}}, \tag{2.16}$$

where the subscript "LM" refers Lorenz-Mie. It is desirable to consider n and expand

the equation to the higher order. However, considering up to $n = \chi + 4\chi^{1/3} + 2$ will yield accurate result. For the cross-sections to be useful as part of the radiative transfer solution, they can be converted to coefficients which are readily used in RTE. The derivations from cross-sections calculated using Lorenz-Mie theory to the corresponding coefficients for two different cases, namely monodisperse and polydisperse, will be the topic of the next subsections.

2.3.2. Monodisperse System

The scattering cross-section of a single particle based on the Lorenz-Mie theory can be used to obtain the scattering coefficient of the medium given that the scatterers are well separated. Hence, the scattering coefficient for a medium consisting of monodisperse scatterers is straightforward to calculate with ISA for a predetermined value of χ and f_v, i.e.,

$$\sigma_{\mathrm{s,ind}} = \frac{f_\mathrm{v} C_\mathrm{sca}(\chi, m)}{V_\mathrm{p}}. \tag{2.17}$$

Here, V_p is the volume of a single spherical particle. The asymmetry parameter can be calculated directly from the Lorenz-Mie theory through the phase function without any modification, as shown in Equation 2.9.

2.3.3. Polydisperse System

The polydisperse particle systems are handled by calculating the sum of the contributions from all radii. Considering a distribution of radii, the scattering cross-section of the entire system can be written as [41]

$$C_{\mathrm{sca,poly}}(m) = \int_{\chi_\mathrm{min}}^{\chi_\mathrm{max}} p\left(\chi\right) C_\mathrm{sca}\left(\chi, m\right) d\chi. \tag{2.18}$$

Here, $p\left(\chi\right)$ is the normalized probability density function of a certain size parameter such that $\int_{\chi_\mathrm{min}}^{\chi_\mathrm{max}} p\left(\chi\right) d\chi = 1$. The value of the asymmetry parameter in the case of

polydisperse spherical scatterers can be calculated as [42]

$$g_{\text{poly}}(m) = \frac{\int_{\chi_{\min}}^{\chi_{\max}} p(\chi)\, g(\chi, m)\, C_{\text{sca}}(\chi, m)\, d\chi}{\int_{\chi_{\min}}^{\chi_{\max}} p(\chi)\, C_{\text{sca}}(\chi, m)\, d\chi}. \tag{2.19}$$

2.4. Dependent Scattering

The dependent scattering effect can be observed in spherical random media which has it scatterers in close proximity with each other. Two of the main ways that are used to predict the quantity of dependent scattering effects will be the topic of discussion here: (1) the direct solution Maxwell's equations for the entire system, more precisely T-matrix method, and (2) the approximate method of SSF.

2.4.1. Direct Solution to Maxwell's Equation

When EM waves propagate through the dense medium, they are incident to a particle ensemble formed inside the particulate media (Figure 2.3a). However, when the T-matrix method (or other methods directly solving Maxwell's equations, e.g., DDA) is used, the incident EM waves approach the particle cloud from free-space as shown in Figure 2.3b. The resulting total scattered field calculated from the T-matrix method can be decomposed into two components, namely, the coherent and incoherent fields. The coherent field is the average component, which represents scattering from free-space - particulate medium boundary. Whereas, the fluctuating component is the incoherent field, which represents diffuse scattering that occurs inside the particulate medium. The latter should be considered for the case of scattering EM waves that are propagating in a dense medium.

The separation of coherent and incoherent radiative characteristics were addressed in Muinonen *et al.* [33]. The processes include; generating N_e number of spherical ensembles similar to what is shown in Figure 2.3b consisting of non-overlapping randomly positioned spherical scatterers, for which the scattering field is estimated using

the T-matrix method. The randomness of the scatterers ensures the satisfaction of the ergodicity hypothesis, which is crucial to correctly represent the incoherent radiative characteristics of the medium.

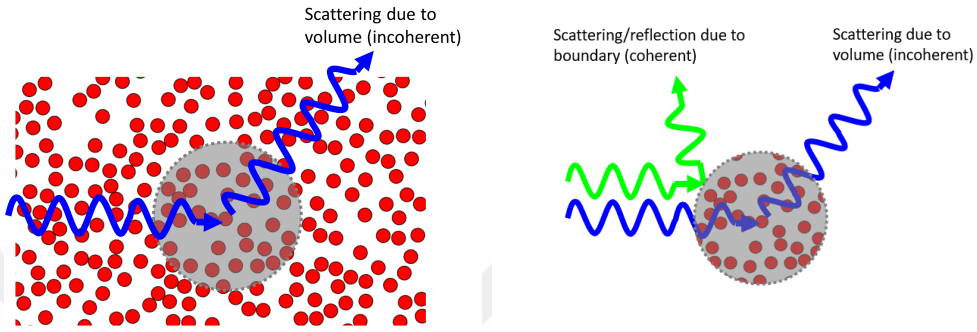

(a) (b)

Figure 2.3. Illustration of EM wave scattering from an ensemble of spheres in (a) particulate medium and (b) free-space. Coherent scattering is observed in the presence of ensemble boundary.

The separation of the coherent electric field from the total electric field is carried out by averaging the values of the total electric field from the different ensembles, which satisfies the Dyson–Schwinger equation, such that

$$\mathbf{E}^{\mathrm{sca,c}} = \lim_{N_e \to \infty} \frac{1}{N_e} \sum_{i=1}^{N_e} \mathbf{E}_i^{\mathrm{sca}}, \tag{2.20}$$

where the scattered electric field for the simulated ensemble i can be represented as

$$\mathbf{E}_i^{\mathrm{sca}} = \sum_{v=1}^{N_0} \sum_{2=-v}^{v} \left(a_{vw1} \mathbf{M}_{vw} + a_{vw2} \mathbf{N}_{vw} \right). \tag{2.21}$$

Here, N_0 is the degree of expansion required to ensure convergence of the result. The $\mathbf{M}_{vw}$ and $\mathbf{N}_{vw}$ are the base vector for vector spherical wave functions and a_{vw1} and a_{vw2} are the coefficients. It is possible to represent these coefficients in terms of T-matrix, which can be written as

$$\begin{pmatrix} a_{vw1,i} \\ a_{vw2,i} \end{pmatrix} = T_i \begin{pmatrix} f_{vw1,i} \\ f_{vw2,i} \end{pmatrix}, \tag{2.22}$$

where the $f_{vw1,i}$ and $f_{vw2,i}$ are the coefficients of the incident electric field of ensemble i given as $\mathbf{E}_i^{\text{inc}}$. Similar to the separation of the electric field into coherent and incoherent parts, the variable T_i can also be separated accordingly, denoted as $T_i = T^{\text{c}} + T_i^{\text{ic}}$. Here, the coherent T-matrix, T^{c}, can be determined by averaging the values of T_i obtained from the calculation of different ensembles, i.e.,

$$T^{\text{c}} = \lim_{N_e \to \infty} \frac{1}{N_e} \sum_{i=1}^{N_e} T_i. \tag{2.23}$$

Obtaining the T_i^{ic} can be done simply by subtracting T^{c} from T_i for each ensemble, in according to the Bethe-Salpeter equation.

The incoherent T-matrix can be used to compute the incoherent electrical field coefficient, similar to Equation 2.22, and in turn, get the incoherent scattering cross-section,

$$C_{\text{sca},i}^{\text{ic}} = \frac{1}{k^2} \sum_{v=1}^{N_0} \sum_{w=-v}^{v} \left(\left| a_{wv1,i}^{\text{ic}} \right|^2 + \left| a_{wv2,i}^{\text{ic}} \right|^2 \right), \tag{2.24}$$

where $k = 2\pi/\lambda$ is the wavenumber. Note that Equation 2.24 can be used as well with total (free-space) scattering cross-section, $C_{\text{sca},i}$, by replacing the two incoherent coefficients with $a_{vw1,i}$ and $a_{vw2,i}$. The extinction cross-section can be obtained in a similar way,

$$C_{\text{ext},i} = \frac{1}{k^2} \sum_{v=1}^{N_0} \sum_{w=-v}^{v} \text{Re}\left(a_{wv1,i} + a_{wv2,i}\right). \tag{2.25}$$

The absorption cross-section is calculated simply by subtracting the scattering cross-section from extinction cross-section, $C_{\text{abs,i}} = C_{\text{ext},i} - C_{\text{sca},i}$. The incoherent extinction coefficient, β_i^{ic}, and incoherent scattering albedo, ω_i^{ic}, can then be obtained, written as

$$\beta_i^{\text{ic}} = \frac{C_{\text{sca},i}^{\text{ic}} + C_{\text{abs},i}}{V_e}, \tag{2.26}$$

$$\omega_i^{\text{ic}} = \frac{C_{\text{sca},i}^{\text{ic}}}{C_{\text{sca},i}^{\text{ic}} + C_{\text{abs},i}}, \tag{2.27}$$

respectively. This study takes an interest in pursuing the radiative characteristics of the medium and the formulation presented thus far has been directly used to compute

them. However, in a typical case where one may require the Poynting vector (which in turn relates to local intensity field), the notion of decoupling between coherent and incoherent field can still be performed, which can be useful, for example, in case of extracting the effective refractive index of the inhomogeneous media [43].

The decoupling of the incoherent and coherent scattered electric fields from total scattered electric field was performed by Yalçın *et al.* [30], and their results are displayed in Figure 2.4. Figure 2.4a illustrates that for low volume fractions, the coherent scattering coefficient component is negligible and total (free-space) scattering consists entirely of incoherent scattering. On the contrary, at high volume fractions, coherent scattering dominates. While the independent scattering coefficient, estimated based on ISA, is similar to the incoherent scattering coefficient at low volume fractions, after $f_{\mathrm{v}} > 0.6\%$ we start to observe a discrepancy, which is in agreement with the early regime map [12, 13]. It is worth noting that Figure 2.4a shows why it is not adequate to use the total (free-space) scattering coefficient as the scattering coefficient for solving RTE. Here, it can be observed that total scattering coefficient overestimating the scattering due to the ensemble - free-space boundary scattering. As a result, we can conclude that using the total (free-space) scattering coefficient as an evaluation metric for establishing the scattering regime map is not an accurate approach.

Figure 2.4b illustrates the coherent and incoherent scattering coefficients for the case with $m = 1.5$ and $f_{\mathrm{v}} = 10\%$ with χ varied. We observe that at low χ, coherent scattering dominates incoherent scattering. As χ increases incoherent scattering becomes dominant, where volumetric scattering within the system dominates over the boundary reflection. While it was not possible to further investigate higher χ due to excess RAM allocation, we expect vanishing of coherent scattering for these higher size parameters. It can be observed at $c/\lambda = 0.5$, the total (free-space) scattering coefficient and the scattering coefficient estimated based on ISA are approaching each other, which may lead to a false interpretation of the demarcation point between dependent and independent scattering regimes. The total (free-space) scattering coefficient estimated for a finite sized ensemble in free-space includes coherent scattering and it

is not physically identical to the scattering coefficient based on ISA that assumes an infinite medium. Therefore the difference should not be used to describe the transition from independent scattering to dependent scattering regime. The demarcation line should have been drawn at the point where the independent and incoherent scattering coefficients intersect with each other, similar to what is observed in Figure 2.4a at $f_v = 0.6\%$. However, in the case presented in Figure 2.4b, the independent and incoherent scattering coefficients do not converge at all, which is a notable observation for us to question the sole use of scattering coefficient as an evaluation metric to draw a demarcation line. Hence, comparing dependent and independent scattering coefficients (or cross sections) will not properly reflect the results of extensive experimental studies reported in [1, 11, 12, 14, 26], which are summarized in Figure 1.1.

In addition to the computational limits, another advantage of pursuing the SSF besides the T-matrix method (IVEGen) is that the latter cannot yield intrinsic characteristics for the scattering direction. It was presented that SSF modifies intrinsic scattering characteristics, i.e., the phase function along with the scattering coefficient, that are obtained from the Lorenz-Mie theory. As a result, these modified quantities can be adopted as scattering characteristics of the medium and can be used directly in RTE solvers such as the MCM. For T-matrix method (IVEGen), as long as there are enough spheres in the ensembles (as in Figure 2.3), increasing the radius of the ensemble will not affect the calculated incoherent scattering coefficient [32] since the scattering coefficient is an intrinsic characteristic. However, this is not the case for the phase function, and in turn, asymmetry parameter. Both scattering coefficient and phase function in T-matrix depend on the ensemble size, and as the ensemble size increases, the ensemble becomes more backscattering, with the corresponding asymmetry parameter becoming smaller. Meanwhile, since SSF directly yields the intrinsic scattering phase function and the accompanying asymmetry parameter for dependent scattering, comparing the phase function (or g) computed with SSF with the ones obtained using ISA will yield more useful information about the effect of dependent scattering than relying solely on the results of the T-matrix method. More on this will be discussed in Section 3.5.

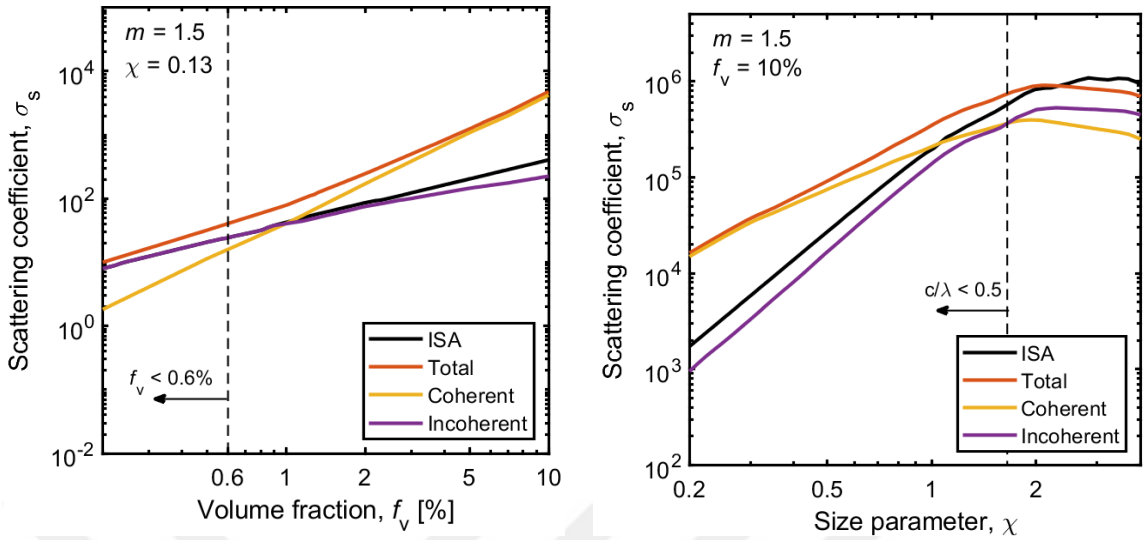

(a) (b)

Figure 2.4. Scattering coefficients as a function of (a) volume fraction at $\chi = 0.13$ and (b) size parameter at $f_v = 10\%$, for a system of randomly dispersed dielectric spherical scatterers with a relative refractive index of $m = 1.5$. Data adapted from the work of Yalçın *et al.* [30].

2.4.2. Static Structure Factor

The interference of radiation scattered by a single scatterer and the neighboring scatterers is one of the major contributors of the dependent scattering. The interference can be represented as a function of relative positions of the neighboring scatterers to a central scatterer. Considering that these scatterers are moving randomly around the central one, the system can be considered as spherically symmetrical, and the relative positions of neighboring particles can then be defined in terms of their relative distances to the central scatter. Similar to statistical mechanics, the radial distribution of the scatterers are then considered and used to estimate a correction to the predictions based on ISA [18], [44,45]. As only far-field interference is considered, near-field effects and plasmon coupling effects cannot be captured by this method.

The effect of the far-field interference can be calculated knowing the phase difference of the scattered wave coming from each particle. Applying the first Born

approximation [46], all particles inside the medium are excited with the incident plane wave, and the total intensity can be formulated as

$$\begin{aligned} I_{\mathrm{s,tot}} &= \left\langle \left| \sum_{i=i}^{N_p} \mathbf{E}_i^2 \right| \right\rangle = \left\langle \sum_{i=1}^{N_p} \sum_{j=1}^{N_p} |\mathbf{E}_i| \, |\mathbf{E}_j| \, e^{i\varphi_i} e^{-i\varphi_j} \right\rangle \\ &= N_p \left|\mathbf{E}_{\mathrm{part}}\right|^2 + \left\langle \sum_{i=1}^{N_p} \sum_{\substack{j=1 \\ j\neq i}}^{N_p} |\mathbf{E}_i| \, |\mathbf{E}_j| \, e^{i\varphi_i} e^{-i\varphi_j} \right\rangle \\ &= N_p I_{\mathrm{s,part}} \left[1 + \frac{1}{N_p} \left\langle \sum_{i=1}^{N_p} \sum_{\substack{j=1 \\ j\neq i}}^{N_p} e^{i(\varphi_i - \varphi_j)} \right\rangle \right]. \end{aligned} \tag{2.28}$$

Here, N_p is the number of particles within the system, $\mathbf{E}$ is the electric field, φ_i is the phase of the wave scattered from the particle i, and the subscript "part" denotes the result of a calculation in a single scatterer configuration. The static structure is encompassed within the square bracket in Equation 2.28. The equation suggests that the total intensity considering dependent scattering effects is calculated by multiplying the independent scattering intensity by the structure factor. The phase difference $\Delta\varphi_{ji} = \varphi_i - \varphi_j$ between the particles is what drives the dependent scattering effect. And to simplify the notation, the static structure factor can be represented as

$$S\left(\theta\right) = 1 + \frac{1}{N_p} \left\langle \sum_{i=1}^{N_p} \sum_{\substack{j=1 \\ j\neq i}}^{N_p} e^{i\Delta\varphi_{ij}} \right\rangle. \tag{2.29}$$

The usefulness of the structure factor in the calculation of scattering characteristics can be demonstrated by how it changes the scattering cross section from the solution of Lorenz-Mie theory, such that

$$C_{\mathrm{sca,dep}} = 2\pi N_p \int_0^{\pi} \frac{dC_{\mathrm{sca,LM}}}{d\theta} S\left(\theta\right) d\theta. \tag{2.30}$$

The asymmetry parameter considering the dependent scattering effects can be obtained as well using $S(\theta)$, and the value is

$$g_{\text{dep}} = \frac{\int_0^{\pi} \Phi_{\text{LM}}(\theta) S(\theta) \cos(\theta) \sin(\theta)\, d\theta}{\int_0^{\pi} \Phi_{\text{LM}}(\theta)\, S(\theta) \sin(\theta)\, d\theta}. \tag{2.31}$$

For ISA, the static structure factor simply converges to unity, i.e., $S(\theta) = 1$.

The calculation of $S(\theta)$ is based on an approximation of the parity of the particles or how the particles are radially distributed within the system. This is represented by a pair or radial distribution function, $f(r^*)$ and its relation with $S(\theta)$ is given as

$$S(\theta) = 1 + 24 f_{\text{v}} \int_0^{\infty} r^{*2} \left[f(r^*) - 1 \right] \frac{\sin(ur^*)}{ur^*} dr^*, \tag{2.32}$$

where $u = (4\pi D/\lambda)\sin(\theta/2)$. Several radial distribution functions can be implemented for the calculation of radiative properties and the gas model, packed-sphere model, liquid model, and hard sphere Percus-Yevick approximations (HSPYA) were used in [13, 18]. HSPYA resembles the pair correlation between hard spheres with no interparticle forces and are non-overlapping with each other [47]. This model is considered to be the most realistic for media consisting of randomly distributed spherical particles. The model has been discussed by Mishchenko [45] and the presented implementation of HSPYA is adopted for the current study.

In HSPYA, the radial distribution $f(r^*)$ function for a case of monodisperse particles can be thought of as such: Consider a realization randomly distributed spherical particles with certain f_{v} and χ shown in Figure 2.5. Consider a distance r^* from the central spherical scatterer (green sphere) and a small distance dr^*. The particles which their centers lie within the confines of the spherical shell produced by r^* and $r^* + dr^*$ (purple spheres) can be counted and recorded. Supposed that the center spheres were chosen differently for sufficiently large Q realizations, the average number of particles within the confines of spherical shell between r^* and $r^* + dr^*$ is [47]

$$\langle P(r^*) \rangle = \frac{1}{Q} \sum_{i=1}^{Q} P_i(r^*). \tag{2.33}$$

Consider if the particles are totally uncorrelated, then the number of particles can be

calculated as

$$\langle P(r^*)\rangle_{\text{unc}} = \frac{\rho(N-1)}{N} 4\pi r^{*2} dr^*, \tag{2.34}$$

where the number density, $\rho = N/V_Q$, is the ratio between the number of particles within the realization and the volume of the generated realization. The factor $4\pi r^{*2} dr^*$ is the volume of the shell. Knowing $\langle P(r^*)\rangle$ and $\langle P(r^*)\rangle_{\text{unc}}$ the radial distribution function can be calculated as

$$f(r^*) = \frac{\langle P(r^*)\rangle}{\langle P(r^*)\rangle_{\text{unc}}}. \tag{2.35}$$

This method of calculating the radial distribution is presented in [47], as a proof to the analytical solution. The current work follows the analytical solution to of the SSF.

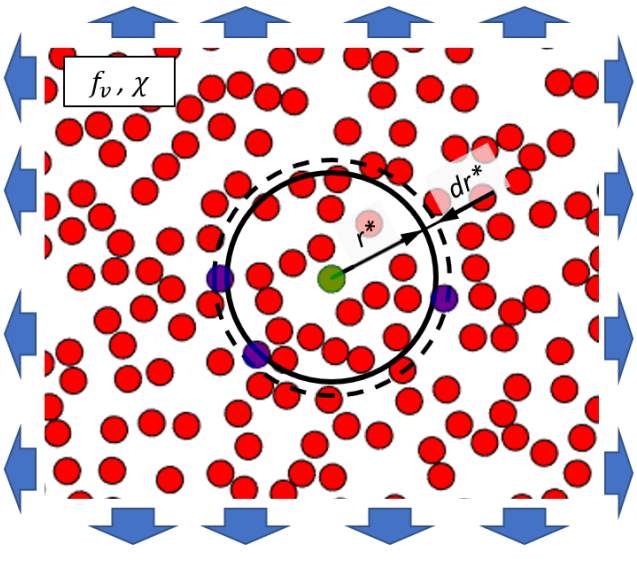

Figure 2.5. Radial distribution of spherical particles, considering the center particle (colored green), and the purple particles are those whose centers lie within the shell confined by r^* and dr^*.

The value of radial distribution in terms of the normalized distance from the spherical scatter is given in Figure 2.6a whereas the structure factor is given in 2.6b. As observed from 2.32a, the curve of radial distribution function changes with different f_v. As HSPYA does not allow for overlapping spheres, the radial distribution between

$0 \leq r^*/D < 1$ is zero, as the distance between two centers of identical spheres that are in contact with each other is D. The value jumps to its peak at $r^*/D = 1$ and then oscillates with a decay. At a sufficiently large distance from the center sphere, the radial distribution becomes unity, suggesting that there are no more correlation between the particles.

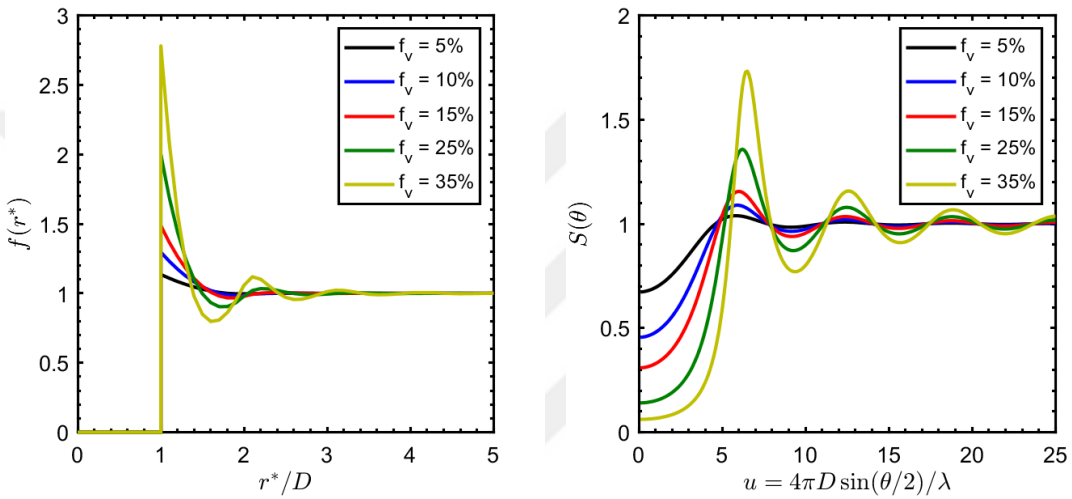

(a) (b)

Figure 2.6. (a) The radial distribution with respect to the distance from the central sphere for different f_{v} (b) Structure factor with respect to u for different f_{v}.

SSF was implemented to ascertain the proposed criteria for the regime map and was shown to yield results that were in good agreement with experimental data [13,18]. This is inline with the study of Yalçın *et al.* [30], which shows that the radiative transfer equation coupled with SSF agrees with the rigorous solution of Maxwell's equations.

3. METHODOLOGY

3.1. Materials

One objective of this study is to identify the effect of material properties on the regime map and establish a conservative map to achieve accurate representations for all cases. For that, we looked into different applications and selected relative refractive indices shown in Table 3.1. It can be seen that the selected cases represent materials with various applications described in the mentioned references.

Table 3.1. Case study and their relative refractive index.

Materials/application	m	Ref.
Air bubble in water	0.751	[48]
Al_2O_3 in polymer binder (infrared)	1.1	[49]
Latex submerged in water (visible light)	1.196	[26]
TiO_2 in polymer binder (infrared)	1.5	[50]
TiO_2 in silica aerogel (visible light)	2.5	[51]
Silicon (Si) in vacuum (infrared)	3.5	[52]

3.2. Dependent Scattering Using Approximation Method

The calculation using Lorenz-Mie theory and subsequent correction with SSF is performed to calculate the radiative characteristics in the presence of dependent scattering. The HSPYA was implemented for the prediction of radial distribution function following the formulation presented in [45]. While the method works well with dielectric particles, it only modifies the scattering terms: scattering coefficient and scattering phase function.The absorption coefficient is not modified since SSF cannot

capture the near-field effects and plasmon coupling. Therefore, absorbing particles, with complex refractive index, are not considered in this study.

3.3. Ensemble Choice for Direct Solution of Maxwell's Equations

Based on the defined volume fraction, size parameter, and ensemble radius, we generate N_e ensembles consisting of randomly distributed monodisperse spherical particles. An accepted practice that will yield correct radiative characteristics starts with generating randomly placed, non-overlapping particles within a cube, whose sides have lengths of L, with periodic boundary conditions applied on each face. An ensemble sampling is carried out by extracting an ensemble with radius R_e from the center of the cube, considering only the particles within that spherical zone (Figure 3.1). This step will then be repeated for N_e times to identify all the needed samples. This procedure produces N_e ensembles with constituent particles varying in number and positions. Considering a sufficiently large N_e, the variation of the number of particles in the ensemble would hover around the mean value $f_\mathrm{v}V_\mathrm{e}/V_\mathrm{p}$ where $V_\mathrm{e} = 4/3\pi R_\mathrm{e}^3$ is the volume of the ensemble. In practice, $L \geq 5R_\mathrm{e}$ and $R_\mathrm{e} \geq 2.5D$ to $10D$, depending on the volume fraction of the case, should be satisfied to achieve ensembles satisfying ergodicity, for a set of χ and f_v. This procedure is implemented through the use of an open source code IVEGen [34].

3.4. Validation and Verification of the Method

Exact solution of light scattering problems are described by Maxwell's equations that govern the propagation of electromagnetic waves based on first principles [8]. The numerically exact T-matrix method can provide the solution of Maxwell's equations and has been widely accepted to find the solution to light scattering problems in a system of spherical scatterers [53]. However, due to the excess RAM allocation, solving Maxwell's equations for the entire range of cases of interest is not possible. Instead, the RTE combined with SSF provides a good approximation for the solution of scattering in a dense medium. A validation study was performed to see if the approximation

holds for a wide range of cases. Figure 3.2a shows the comparison of the scattering coefficient as a function of size parameter calculated by the two methods for a case with the scatterers' relative refractive index of $m = 1.196$ and with two different volume fractions, namely, a case with a relatively disperse particulate media $f_v = 10\%$ and a more dense $f_v = 25\%$. It is interesting to note that the scattering coefficient from the two different volume fractions almost coincide with each other. This suggests that the approximation made by SSF, that ignores the near-field effect, is valid for the case where dielectric material is considered. The observed agreement between SSF and the T-matrix method (IVEGen) provides confidence for the use of SSF.

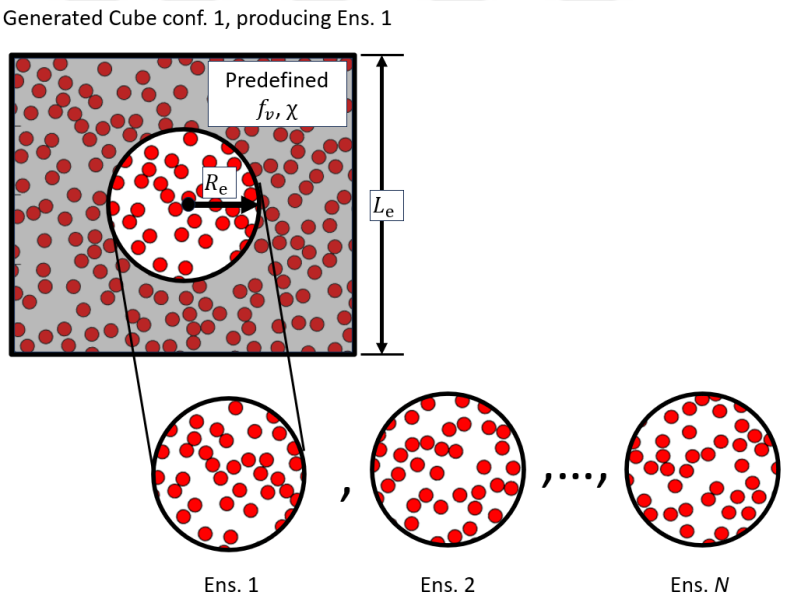

Figure 3.1. The process of ensemble generation. Starting with generating a cube with sides of L_e, occupying the cube with particles of predetermined χ and f_v and taking a spherical ensemble from the center with the radius of R_e. The processes are repeated until N number of ensembles are produced.

Figure 3.2b shows the calculated and measured normal-hemispherical transmittance, T_{nh}, for a colloidal suspension that was previously presented in [30]. The experimental setup consists of suspension with a thickness of 10 mm composed of polydisperse silica nanoparticles of log-normal distribution in water with a mean radius of 10.1 nm

and a standard deviation of 0.2 in varying volume fractions from 2% to 15%. The suspension was illuminated with light having a wavelength of $\lambda = 500$ nm, which would make the average size parameter of the case, $\chi = 0.13$. It is clear from the figure, that the approach based on ISA severely underestimates the T_{nh} value, especially at high f_{v} compared to experimental measurements. Moreover, the calculation of radiative transfer with SSF is in agreement with the more rigorous method R^2T^2, which accounts for both near-field and far-field effects.

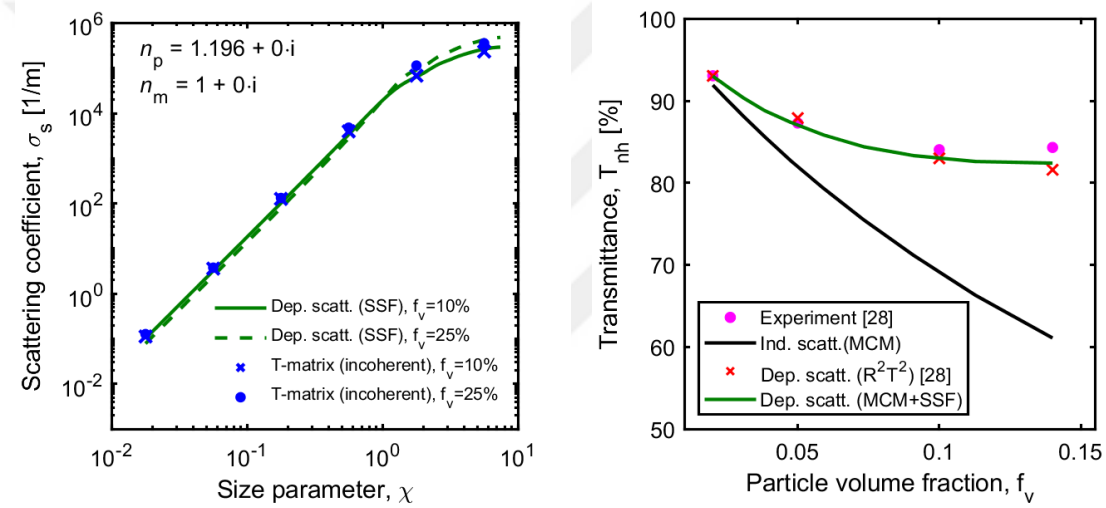

(a) (b)

Figure 3.2. Verification and validation of SSF through (a) scattering coefficient ($f_v = 10\%$ and 25%, varying χ) (b) theoretical calculation of normal-hemispherical transmittance and comparison with the available experimental value from [30] where the radius of the particles within the medium follows the log-normal distribution with a mean of 10.1 nm and standard deviation of 0.2 and $\lambda = 500$ nm ($\chi_{\text{avg}} = 0.13$).

3.5. Challenges in Solving the Maxwell's Equations for Regime Map

The direct EM solution covers more phenomena than SSF such as near-field effect and coherent back-scattering. The apparent problem in the attempts by different authors was that when they approached the problem by directly solving Maxwell's equations for the entire system (e.g., using the T-matrix method and DDA), they

overlooked coherent scattering while calculating the scattering cross-section of particle ensembles [23, 24], [31]. Coherent scattering coefficient can be identified and then be deducted from the total(free-space) scattering coefficient by applying the procedure described in Section 3.3. The deduction will result in the incoherent scattering coefficient which is the relevant scattering coefficient to use when solving the RTE. The scattering regime map can then be drawn, considering the deviation of the incoherent scattering coefficient, calculated using T-matrix, from the prediction using ISA, which was attempted recently [54]. However, the study did not consider the directionality of the scattering, and resulted in an outcome that is inconclusive. This is a problem that is addressed in this study by accounting for the contribution from the phase function.

However as discussed in Section 2.4.1, both the scattering coefficient and the phase function obtained from T-matrix changes with the ensemble size. A scattering problem involving spherical ensembles of varying sizes filled with spherical scatterers with $m = 1.196$ and $\chi = 1$ was performed (Figure 3.3). The volume fraction was kept relatively high, at $f_v = 25\%$, to give a clear demonstration on how ensemble size affects both the scattering coefficient and, more prominently, the phase function. Figure 3.3a shows the phase function calculated using Lorenz-Mie theory, with and without SSF, and T-matrix with varying ensemble sizes. The relatively high volume fraction significantly affects the phase function, as evidenced by the difference between the phase function calculated using only Lorenz-Mie theory and the one that includes the contribution from SSF. The former exhibits predominantly a forward scattering behavior, while the latter shows the opposite. The trend is a more backscattering phase function with the increase of the ensemble size, meaning than a decrease in g as the ensemble size grows. A better observation on the effect of ensemble size to the asymmetry parameter can be made by looking to Figure 3.3b. A consistent decrease in g can be seen throughout the presented ensemble sizes, and the decrease is predicted to continue pass the range that is given, as more particles are added. The scattering coefficient shown in the same figure also decreases with the increase in ensemble size, albeit at a different rate considering the logarithmic scale used to represent the value.

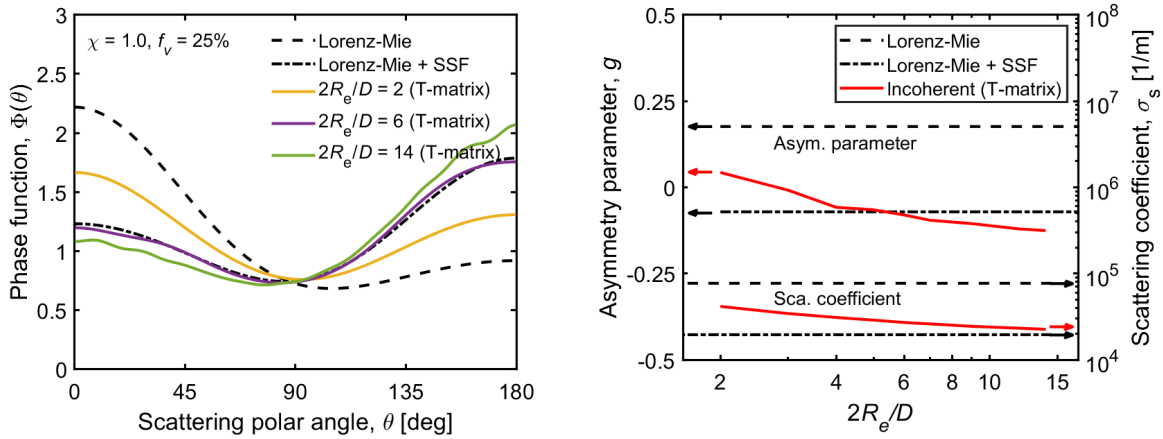

(a) (b)

Figure 3.3. (a) Phase function for the case of $f_v = 25\%$ and $\chi = 1$ performed using three different methods, i.e., Lorenz-Mie theory, both with and without SSF, and T-matrix. Ensemble size presented as the ratio between ensemble diameter to the particle diameter ($2R_e/D$). (b) Asymmetry parameter and scattering coefficient computed using the same three different methods for varying ensemble size.

Figure 3.4 presents the same case of $m = 1.196$, $\chi = 1$, and $f_v = 25\%$, but focusing on the difference in quantity between prediction made using T-matrix and that of SSF. The relative difference in scattering coefficient is presented as

$$E_\sigma^{\mathrm{Tm-SSF}} = \left| \frac{\sigma_\mathrm{s}^{\mathrm{Tm}} - \sigma_s^{\mathrm{SSF}}}{\sigma_\mathrm{s}^{\mathrm{SSF}}} \right|. \tag{3.1}$$

Here, the superscript "Tm" and "SSF" are used to indicate the value calculated using T-matrix method and SSF, respectively. The absolute difference of g calculated using T-matrix and SSF is defined as

$$E_g^{\mathrm{Tm-SSF}} = \left| g^{\mathrm{Tm}} - g^{\mathrm{SSF}} \right|. \tag{3.2}$$

Absolute difference was taken for g considering that asymmetry parameter already is a bounded quantity, which has a range between -1 and 1. Taking the relative difference will results in amplified quantity in the case where g is close to 0. The value was multiplied by a factor of ten to improve clarity, and to fit both the difference in σ_s and g into one figure. It is shown that $E_\sigma^{\mathrm{Tm-SSF}}$ exponentially decays with the increase

in ensemble size. It is predicted that eventually, the value will become small enough as the size goes to infinity, effectively making SSF a valid tool to predict the value of scattering coefficient. The asymmetry parameter did not follow the same trend, and the difference reached a minimum point before rising again afterwards. Thus, this finding supports the claim made before in Section 2.4.1 that the SSF provides more valuable information to understand the effect of dependent scattering to the phase function, considering that the phase function calculated using T-matrix always increases with the size of the ensemble and do not converge to any value. Thus, in the next sections, the quantities that consider dependent scattering (e.g., $\sigma_{s,dep}$, $\sigma'_{s,dep}$, and g_{dep}) are calculated using SSF, unless otherwise specified.

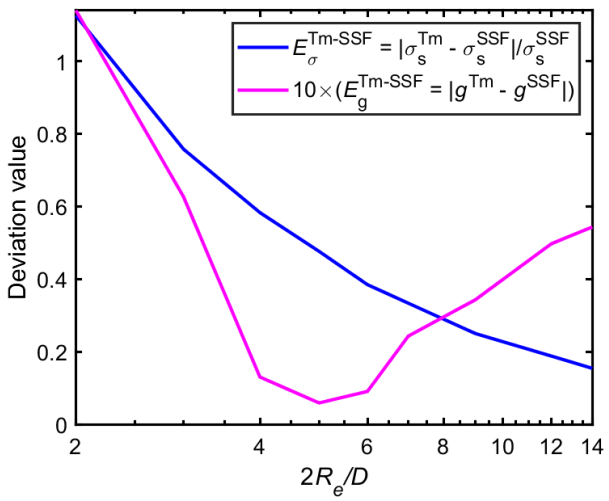

Figure 3.4. Difference between the result calculated with T-matrix and one that is calculated with SSF for the case of scattering coefficient and asymmetry parameter. A factor of 10 was multiplied to the result of the difference in the asymmetry parameter only to improve clarity so that it fits in the same graph as the result of the scattering coefficient

3.6. Calculation of Deviation

The deviation of the radiative characteristics from those calculated considering ISA had been used before to determine if a dependent scattering effect is present

[12–14, 18]. In regards to the scattering coefficient, the deviation of the ISA solution from a more accurate result considering dependent scattering can be defined as

$$E_{\sigma} = \frac{\sigma_{\mathrm{s,ind}} - \sigma_{\mathrm{s,dep}}}{\sigma_{\mathrm{s,dep}}}. \tag{3.3}$$

Similar to the scattering coefficient, the transport scattering coefficient can also be used as an evaluation metric, In regards to σ'_{s}, the deviation can be defined as

$$E_{\sigma'} = \frac{\sigma'_{\mathrm{s,ind}} - \sigma'_{\mathrm{s,dep}}}{\sigma'_{\mathrm{s,dep}}}, \tag{3.4}$$

and for the asymmetry parameter,

$$E_g = g_{\mathrm{ind}} - g_{\mathrm{dep}}. \tag{3.5}$$

Note that the difference of asymmetry parameters is taken directly, without any normalization. If relative deviation were to be used, the asymmetry parameters close to 0 (nearly isotropic scattering), would have amplified the deviation. Moreover, unlike the scattering coefficient, the lower and upper limits of the asymmetry parameter are defined, which are -1 for the case of full back-scattering and 1 for full forward-scattering.

Similar to the earlier works [12–14], [18], reflectance is also considered as an evaluation metric. Since its lower and upper bounds are known and it is already a relative term by definition, an absolute deviation is used as a metric. Normal to hemispherical Reflectance obtained using MCM while considering ISA uses the symbol $R_{\mathrm{nh,ind}}$, whereas one that include SSF uses $R_{\mathrm{nh,dep}}$, and the deviation is given by

$$E_R = R_{\mathrm{nh,ind}} - R_{\mathrm{nh,dep}}. \tag{3.6}$$

4. RESULT AND DISCUSSION

4.1. Evaluation of Scattering Coefficient and Asymmetry Parameter

Figure 4.1a and b show the resulting discrepancies in the scattering coefficient and asymmetry parameter, respectively, between predictions considering dependent scattering and ISA. The plots are for the case, $m = 1.196$, representing dielectric latex particles submerged in water, which is widely studied experimentally and numerically in the literature [1], [12–14], [18]. The figures follow the format of the early regime maps outlined by the studies conducted in the 1980s. The separating line of independent and dependent scattering in the work of Drolen *et al.* [12] is presented as a black dashed line to provide a comparison between the early work and the current work based on computed deviation value as described in Section 3.6. Additionally, the points within the region of the map, where Mishchenko *et al.* [26] did their experimental work, are also presented as their work provides the major motivation for the reevaluation of the regime map. The colors of the symbols provide information on validity of the ISA in calculation of the reflectance as outlined in [26]. Here, green indicates ISA is valid and in good agreement with experimental data, yellow indicates that the ISA should be used with caution, and red indicates that ISA is not applicable. So far, studies on the scattering regime map have relied on a limited number of data points to assess the proposed criteria [1], [14], [12], [23, 24]. To address this limitation, the current study covers the entire regime map of interest and draws the isolines of deviation. The detail of how the coverage of the map was done is presented in detail in the supplementary material along with how the data points taken within the map changes the isolines of deviation that are produced.

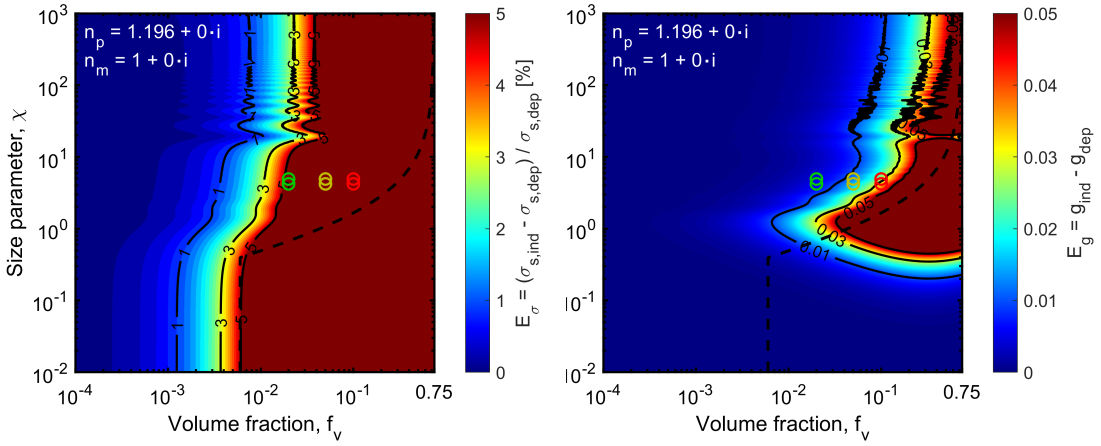

(a) (b)

Figure 4.1. Deviation value in terms of the (a) scattering coefficient (b) asymmetry parameter calculated using SSF for varying volume fraction and size parameter. Demarcation line from Drolen *et al.* [12] is given. The experiments from [26] is marked by green (ISA is valid), yellow (ISA should be used with caution), and red (ISA is invalid) open circles.

The 5% deviation from scattering cross section has been used extensively in studies to conclude whether dependent effect prevails [12], [14], [18], [23,24]. Following the same approach, it is observed that the deviation, $E_\sigma = 5\%$, calculated based on σ_s shown in Figure 4.1a follows the feature of the early regime map in the dilute case, i.e., $f_v < 0.6\%$, indicated by the vertical line, where it is found that the scattering is always independent. This feature has been proven to be true experimentally when Drolen *et al.* [12] investigated particles in the size parameter, $\chi = 0.205$. In fact, SSF has been confirmed to give a reasonably good agreement with the experimental data for the relatively small size parameter $\chi = 0.205$ with varying f_v. Although the map in Figure 4.1a captured this phenomenon at low size parameters well, it cannot explain why the early experimental result relying on the observation of extensive properties (i.e., reflectance and transmittance) has proven that ISA would still give a good result at relatively high size parameters, $\chi \approx 10$ and beyond. Thus, an evaluation based on σ_s alone to assess the validity of or transition between the independent and dependent regimes is deemed not suitable. This result was foreseen as in our previous study [30] (Figure 2.4b) where

a non-vanishing gap between independent and incoherent scattering coefficients with increasing size parameter was observed.

Figure 4.1b shows the deviation based on the difference in the asymmetry parameters, E_g. The 0.05 deviation line from the difference between g calculated using ISA and SSF shows a relatively close alignment with the early transition criterion, $c/\lambda = 0.5$. Moreover, the results of the experiments by Mishchenko *et al.* [26] has shown agreement with Figure 4.1b, as the two cases where dependent scattering prevailed represented in red dots are close to the border of the 0.05 isoline. However, it cannot be overlooked that the region of $f_v \geq 0.6\%$ for low χ, which has been proved to be in the dependent scattering regime, would be depicted as independent if E_g is used as the criterion of transition. Hence, the sole use of g to demarcate the independent and dependent scattering regimes is not adequate as well.

4.2. Evaluation of Reflectance and Transport Scattering Coefficient

An evaluation based on neither σ_s nor g, alone effectively differentiates between dependent scattering and independent scattering raises a new question: Is there another parameter that could better delineate the boundaries between the regimes of independent scattering and dependent scattering?

Following the 5% deviation trend set by previous studies, we experimented on using the transport scattering coefficient since it can be used as the sole scattering characteristic in RTE as explained in Section 2.2.2. The current study covers the entire regime map of interest for the case of $m = 1.196$ and draws the isolines of deviation, $E_{\sigma'}$, which is shown in Figure 4.2. Included in Figure 4.2 are the points where Mishchenko *et al.* [26] conducted their experiments, represented by the colored open circles, and the demarcation line based on [13], represented by the dashed line. Note that the red open circles, representing experiments, where ISA is not applicable, are within the confines of $E_{\sigma'} = 5\%$, meaning that this metric yields consistent results with the latest experiments. Furthermore, the separation of the regimes by a vertical

line at $f_v = 0.6\%$ for the case of low size parameter, i.e., $\chi < 0.4$, was also observed, consistent with the early studies [12], [18].

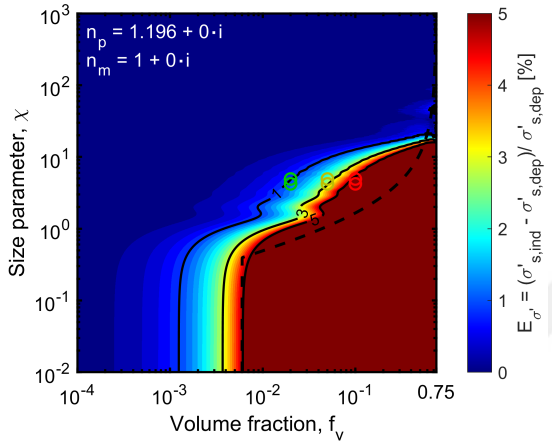

Figure 4.2. Calculated deviation considering the transport scattering coefficient as a function of f_v and χ along with experimental data points from [26] shown as colored open circles and early transition criteria (black dashed line) from [12].

Further studies were conducted to prove that the agreement observed for the results based on the transport scattering coefficient is not a mere coincidence and not limited to certain points/regions. In many science and engineering applications, the focus is on the intensity field and properties such as transmittance and reflectance that are easy to measure are of practical importance. Thus any parameter used to separate between independent/dependent scattering should follow the trend set by the intensity field. To prove if the transport scattering coefficient is following the trend of intensity field, we conducted a study with $m = 1.196$, $f_v = 10\%$ following the experiments in [26], with varying χ. The results are presented in Figure 4.3 for a plane-parallel suspension with a thickness of 50 μm, showing the variation in σ_s, g, R_{nh} and σ_s'. The two vertical red lines represent the experimental data points by Mishchenko *et al.* [26], which are presented by two red open circles in Figure 4.1. The black dashed line representing $c/\lambda = 0.5$ is shown as a reminder of the criteria proposed by the early regime map [12]. Note that the experiments were in the region $c/\lambda > 0.5$, which would classify the experimental data to be in the independent scattering regime according

to the regime map although the dependent scattering effects were observed in the lab measurements [26]. In Figure 4.3a, the σ_s considering ISA and dependent scattering effects was not observed to converge as the size parameter increases. More clearly, it is shown by the deviation plot given at the bottom of the figure, where the deviation was persistently above 10%. This is consistent with the observation presented in [30], which is shown in Figure 2.4b, and even for $\chi > 10$ this phenomenon is still valid. The same trend was observed for the value g as well in Figure 4.3b. Note that independent scattering is expected to prevail at high χ according to what was reported in [1, 14]. From Figure 4.3c and d, it is obvious that there is a similarity in the convergence trends of R_{nh} and σ'_{s}. Both properties increase monotonically until χ reaches approximately 1.5, followed by a slightly oscillating increase, and then decrease when χ reaches 4. Unlike Figure 4.3a and Figure 4.3b, the value of R_{nh} and σ'_{s} estimated based on ISA and SSF that captures dependent scattering effects, converges from $\chi \approx 10$ and beyond, which is shown at the bottom figure of each where the deviation goes below 0.01 and 1% respectively for E_R and $E_{\sigma'}$. To further emphasize, the similarity between Figure 4.3c and d from how the deviation values converge closely to 0, give indication that σ'_{s} follows the trend set by the intensity field, whereas σ_{s} and g do not.

Further studies to investigate the connection between transport scattering coefficient and reflectance were conducted, now covering the entire regime map. The simulations rely on the Monte Carlo solution to radiation incident to a parallel plane-parallel slab similar to the case presented in Figure 4.3c. However, maintaining the thickness of the slab to a certain value for the entire region renders part of the regime map with low f_{v} and low χ overlooked due to the resulting small or large optical thickness. The sensitivity of reflectance to scattering properties varies significantly with changing optical thickness. Such variances must be avoided as transition between dependent and independent scattering is usually defined in terms of a predetermined deviation in predicted properties. Here, instead of constant thickness, an alternative approach based on an inverse solution procedure is utilized to ensure the calculated deviation based on reflectance has similar sensitivity throughout the entire regime map.

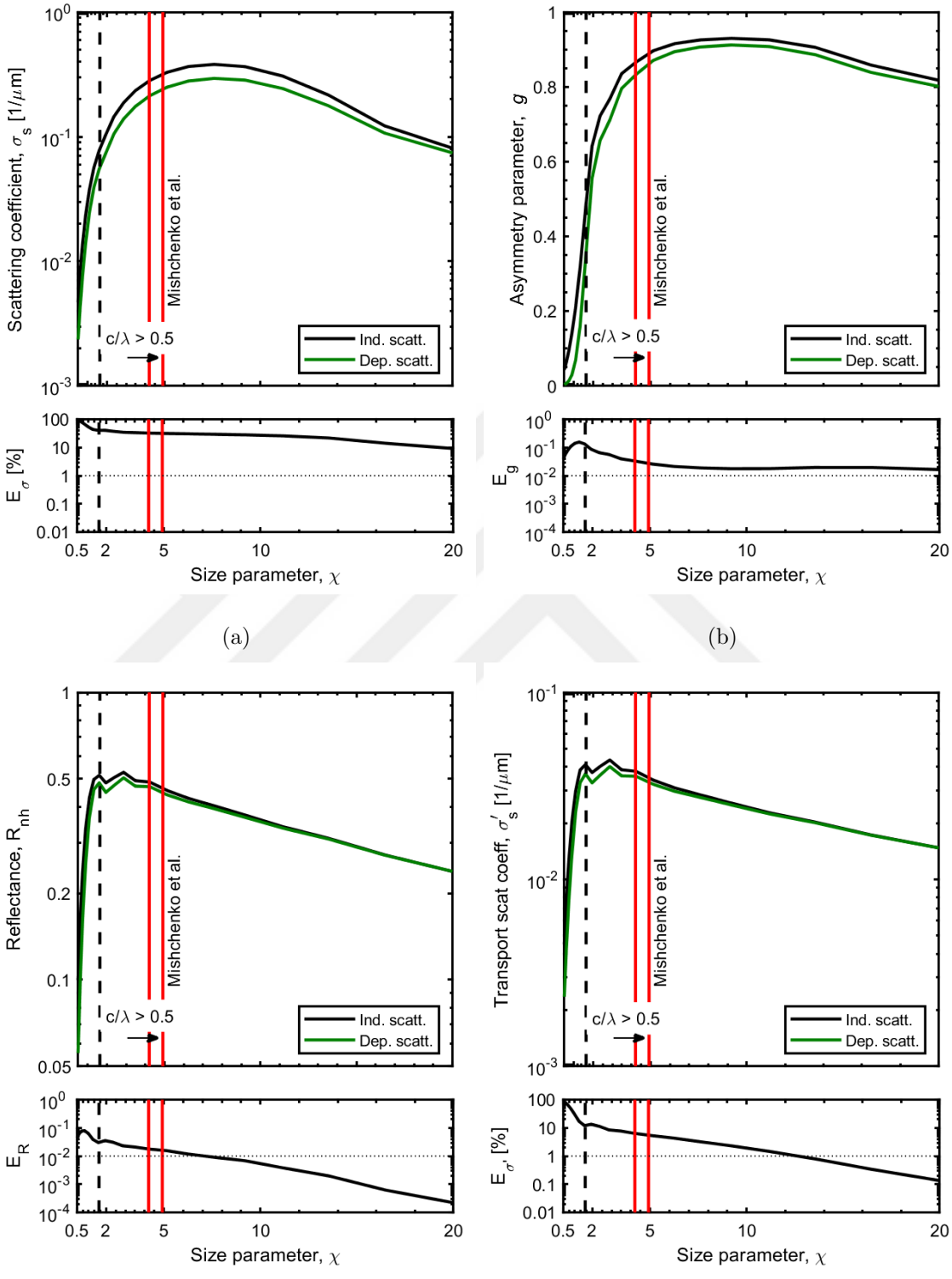

Figure 4.3. Independent and dependent scattering cases are simulated at $m = 1.196$ and $f_v = 10\%$ for the value of (a) scattering coefficient (b) asymmetry parameter (c) normal-hemispherical reflectance (d) transport scattering coefficient, accompanied with the deviation values.

The approach relies on utilizing a constant value of reflectance when dependent scattering is considered, $R_{\mathrm{nh,dep}}$ = const., throughout the regime map. This is accomplished by solving the inverse problem of identifying the thickness of the slab, $L(R_{\mathrm{nh,dep}})$, for satisfying a predetermined reflectance, $R_{\mathrm{nh,dep}}$. Here, the solution of RTE with SSF for each case defined by a pair of f_{v} and χ values is calculated. For the current study, $R_{\mathrm{nh,dep}}$ was chosen to be 0.1, 0.25, 0.5, 0.65 and 0.8 and the calculated thicknesses along the map are then used to simulate RTE with ISA for predicting reflectance, $R_{\mathrm{nh,ind}}$. The deviation between $R_{\mathrm{nh,ind}}$ and $R_{\mathrm{nh,dep}}$, referred as E_R as shown in Equation 3.6, are then calculated for the entire map. The corresponding $L(R_{\mathrm{nh,dep}})$ values throughout the regime map are presented in the Supplementary Materials.

Figure 4.4a shows different E_R for different $R_{\mathrm{nh,dep}}$ values to show the consistency of the approach across the predetermined reflectance values. The selection of E_R lines of each different reflectance was based on, achieving the best fit with the vertical demarcation line of $f_{\mathrm{v}} = 0.6\%$ at $\chi \leq 0.4$. Here, it is shown that similar behavior is observed for all different constant reflectance values at the corresponding E_R. The fluctuating pattern around the mean value observed for each of the isolines of deviation is related to the statistical uncertainty inherent in MCM. The isoline of deviation of $E_{\sigma'} = 5\%$ matching those formed by E_R was expected, considering that our study presented in Figure 4.3c and d indicate that there is a similarity in the trend of the two deviation values. Overall, it can be observed that a relatively good fit is achieved among all the data presented, and the highest deviation is observed for $R_{\mathrm{nh,dep}} = 0.5$ at E = 0.012 (detail of the plot is given in Figure 4.4b). The similarity include the vertical demarcation line at low χ and the region of independent scattering at relatively high χ. Thus, by covering the entire region, we have confirmed that the transport scattering coefficient follows the trend set by the intensity field.

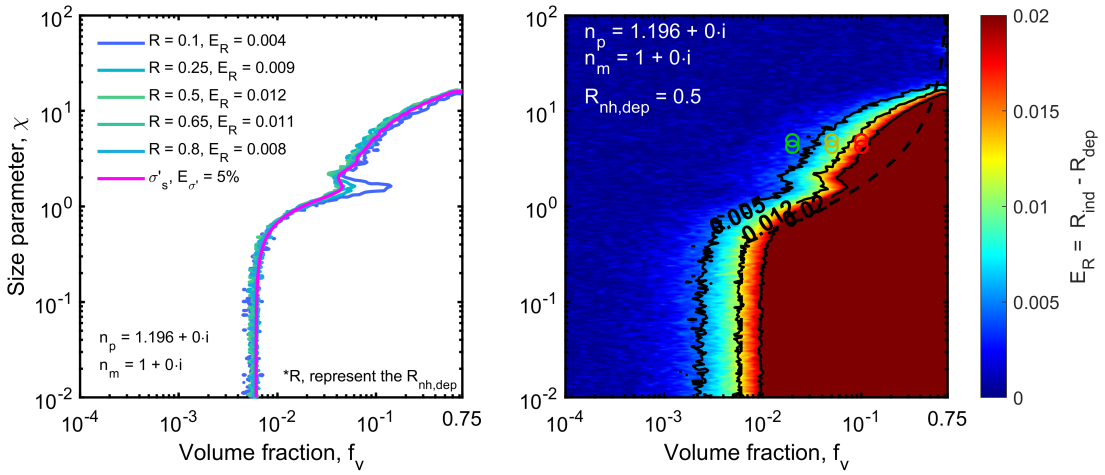

(a) (b)

Figure 4.4. (a) isoline of deviation based on transport scattering coefficient, i.e., $E_{\sigma'} = 5\%$, accompanied by isolines of deviation for different $R_{\mathrm{nh,dep}}$ and c/λ=const. lines. (b) E_R for the case when $m = 1.196$ and the $R_{\mathrm{nh,dep}} = 0.5$.

4.3. Effect of Polydispersity and Refractive Index

The case of regime map with $m = 1.196$ has been considered thoroughly and there are abundance of experimental studies to support [1], [12], [14], [26]. The features of regime map with $m = 1.196$ has been discussed in the previous subsection as well. To incorporate relative refractive index into the regime map, the the lines of $E_{\sigma'} = 5\%$ produced with various values of m must be obtained. The same procedure to generate $E_{\sigma'}$ isolines of deviation in the previous subsection is applied for a system of particles with $m = 1.5$ (Figure 4.5a). Changing the relative refractive index to 1.5 generate strong oscillations of $E_{\sigma'}$. This oscillation starts at around $\chi = 1.5$ and becomes significant at $\chi > 7$. The oscillations observed in the figure are the result of interference in the EM field. These interferences are not observed in experiments due to two major reasons. Firstly, monodisperse particles are considered in the analysis, whereas the particles in experiments are polydisperse with a particle size distribution [45]. Moreover, there is also a variation of the refractive index inside the particles due to imperfections that inherently prevent interferences, especially for large particles. Monodisperse systems of particles with no imperfections are considered in the analysis

and with neither polydispersity nor the refractive index variation considered, it would be normal to observe these oscillations due to interference, especially at high size parameters, i.e., $\chi \geq 10$. Figure 4.5b presents the results for a polydisperse system of particles, whose particle size distribution is defined based on a log-normal distribution with a standard deviation, SD $= 0.2$ following the previous study [30]. It can be observed that the oscillations due to interference wanes, yielding the average values of the oscillating pattern. Although there will always be variations in particle size within the system, imperfections in the shape of the grains, and/or variations in refractive index due to imperfections in practice [55, 56], only polydispersity is considered in the upcoming discussions.

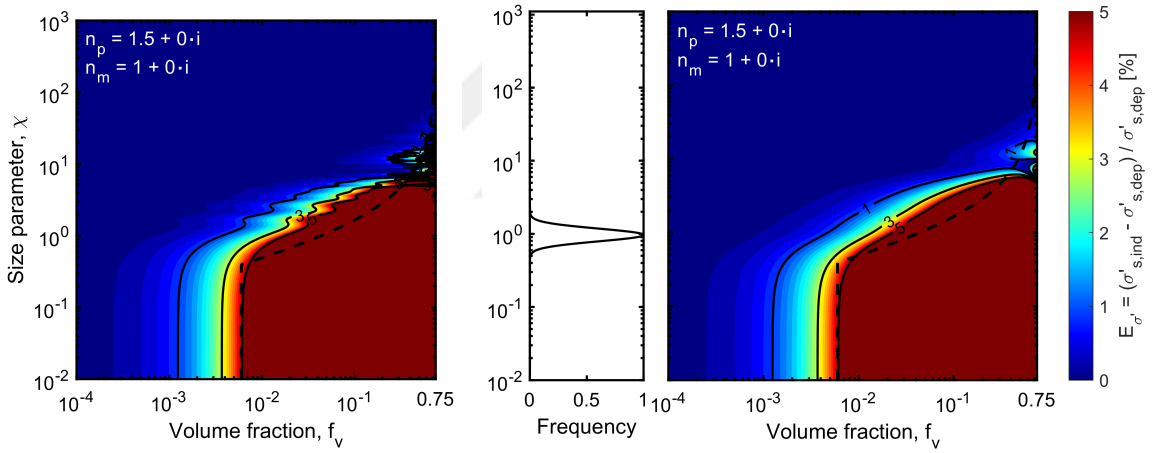

(a) (b)

Figure 4.5. Calculated deviation considering the transport scattering coefficient as a function of f_v and χ at $m = 1.5$ considering (a) monodisperse and (b) lognormal polydisperse particle size distribution with SD $= 0.2$. The particle size distribution diagram for the case when $\chi = 1$ is presented as well.

Computation of $E_{\sigma'}$ for a system of log-normal polydisperse particles with SD $=$ 0.2 is carried out for two different refractive indices, $m = 1.1$ and 3.5, and the results are shown in Figure 4.6a and b, respectively. It can be directly observed that the two refractive indices produce different isolines of deviation although they still retain some of the prominent features that were established earlier in the region $\chi \leq 0.4$, which is

largely under the dependent scattering except for $f_v \leq 0.6\%$ [12] and $\chi \geq 50$, which is entirely under the independent scattering [1,14,18]. Additionally, contrary to [24], it is observed that optically soft scattering medium consisting of low refractive index scatterers, such as $m = 1.1$, will result in a regime map where dependent scattering effects are effective over a relatively larger region. On the other hand, for scattering media with high refractive index mismatch (Figure 4.6b), the demarcation line converges to the line of the early regime map. Moreover, the region in which Mishchenko *et al.* [26] carried out their experiment varies between the dependent and independent scattering based on the refractive index mismatch. Therefore, building a regime map without considering different refractive indices, as in the case of early literature [1, 12, 14], will result in overlooking a region that is frequently used in various applications, where dependent scattering effects are observed.

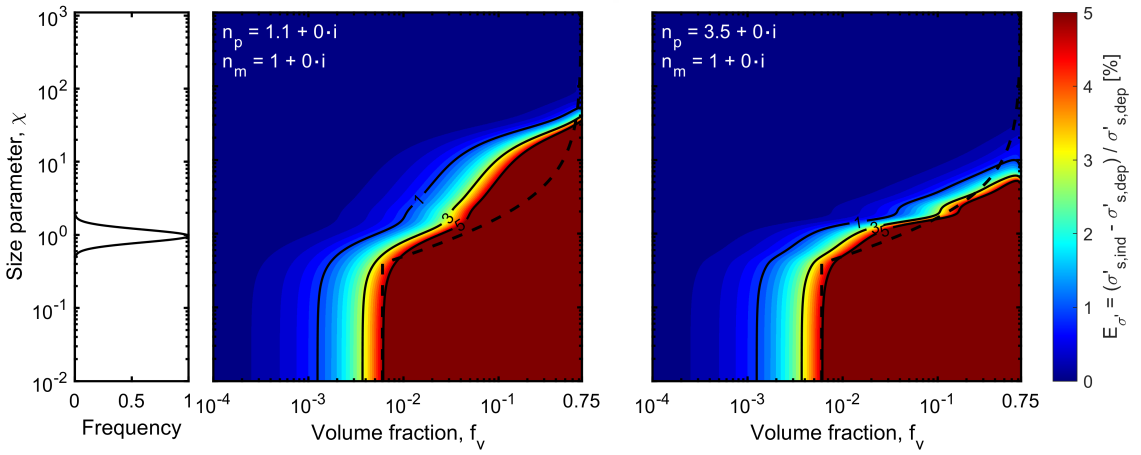

(a) (b)

Figure 4.6. Calculated deviation considering the transport scattering coefficient as a function of f_v and χ, for polydisperse particles with SD = 0.2 at (a) $m = 1.1$ (b) $m = 3.5$. The distribution follows the case in Figure 4.5b.

4.4. Proposed Regime Map

Figure 4.7a shows a series of $E_{\sigma'} = 5\%$ from different refractive indices, namely, 1.1, 1.196, 1.33, 1.5, 2.5, and 3.5. Alongside the isolines of deviation, included in the

figure, a vertical line of $f_v = 0.6\%$ is connected to two different c/λ =constant lines. Of these, $c/\lambda = 0.5$ is the demarcation line of the early regime map [13], whereas $c/\lambda = 2$ is the proposed demarcation line considering the transition from independent to dependent scattering. This line conservatively captures the region where dependent scattering effects are valid, with the exception of a slight zone where it interferes with the line for $m = 1.1$ case.

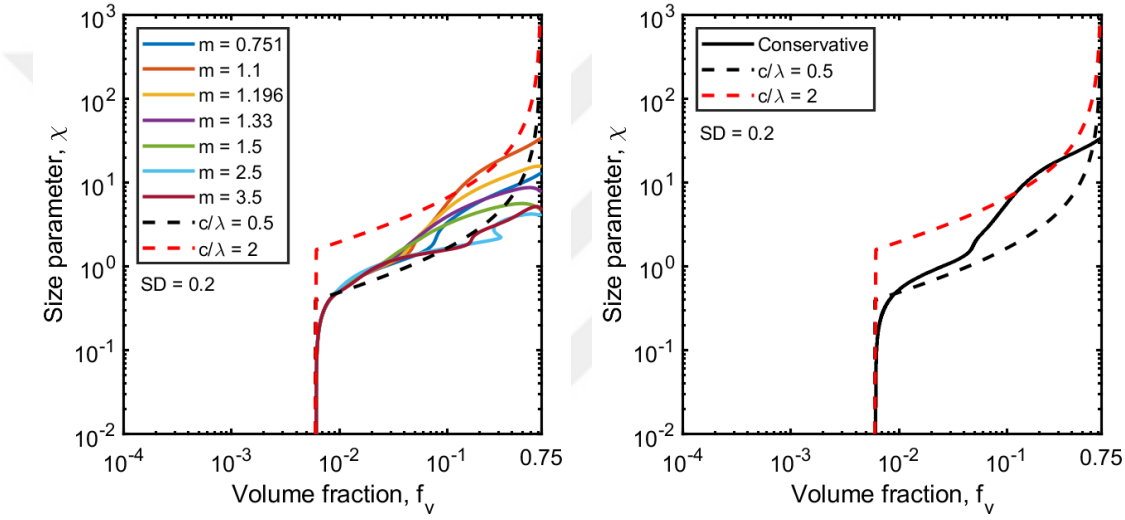

(a) htbp (b) htbp

Figure 4.7. $c/\lambda = 0.5$ and 2 alongside (a) 5% deviation lines from polydisperse particles with SD = 0.2 at different relative refractive indices, namely, m = 1.1, 1.196, 1.33, 1.5, 2.5, and 3.5. (b) Proposed regime map considering the most "Conservative" criteria of the cases illustrated in (a).

5. CONCLUSION

5.1. Summary and Conclusions

In the current study, the scattering regime map is revisited. Unlike previous studies, which relied on selectively considering a limited number of regions within the regime map and concluding a separation line from those limited data; the current study exhaustively investigates the entire region within the regime map, point-to-point, that is of interest for most applications. A proper evaluation metric for determining the demarcation line is sought by considering the deviation of different radiative properties from the solution that takes into account dependent scattering effects. The chosen metric was set so that it follows the trend of the intensity field, which was covered by making reflectance study over the entire regime map. Transport scattering coefficient is found to be the proper intrinsic property for capturing the dependent scattering effects as it is capable of reflecting the dependent scattering effects in intensity field.

Several features that were observed from the early regime map are ascertained in the current study. First, consistent with previous theoretical and experimental studies, the existence of a vertical separating line at low size parameters is also acknowledged in the current study. Thus, for a system of random spherical scatterers with a volume fraction less than 0.6%, it would be predicted that independent scattering prevails, regardless of the size parameter. Second, for very high size parameters exceeding 50, it is safe to assume independent scattering to prevail entirely.

It is found that variations in the refractive index also lead to slightly different regime maps. The identified regime map based on the transport scattering coefficient will align more with the early regime map for larger refractive index mismatch between particle and medium. On the other hand, for a lower refractive index mismatch the dependent scattering zone expands slightly and as a result the corresponding regime maps for smaller refractive index mismatch are more conservative, especially at the

regions where size parameter is larger than one. Finally, for the most conservative scenario, a modification to the regime map can be done by disregarding the relative refractive index and replacing the $c/\lambda = 0.5$ line with $c/\lambda = 2$ line.

5.2. Recommendation for Future Works

This thesis discusses the regime map in the limited case of spherical particles and dielectric materials. While this study may provide valuable insights for a wide range of applications, there is still merit in studying a broader range of shapes or materials to observe their effects. Exploring variations in shape (fibers, disks, rods, etc.) may yield different demarcation lines on the regime map. Another limiting factor of this study is the use of the static structure factor to account for the dependent effect. This method only considers far-field interference and cannot account for near-field effects and plasmon resonance. It is most interesting to study these effects while considering metallic materials with complex refractive indices. Furthermore, the demarcation line produced in this study, although it was made after thoroughly considering the entirety of the region of interest and with a wide variety of conditions, lacks experimental verification. Given that, in real-world applications, agglomeration is a common occurrence (especially in charged nanoparticles [57]), the effect could potentially change the regime map significantly [58]. Thus, significant opportunities remain for further expansion of this research.

REFERENCES

1. Brewster, M. Q. and C. L. Tien, "Radiative Transfer in Packed Fluidized Beds: Dependent Versus Independent Scattering", *Journal of Heat Transfer*, Vol. 104, No. 4, pp. 573–579, 11 1982.

2. Orel, B., M. Gunde, and A. Krainer, "Radiative Cooling Efficiency of White Pigmented Paints", *Solar Energy*, Vol. 50, No. 6, pp. 477–482, 1993.

3. Haapanala, P., P. Räisänen, G. M. McFarquhar, J. Tiira, A. Macke, M. Kahnert, J. DeVore, and T. Nousiainen, "Disk and Circumsolar Radiances in the Presence of Ice Clouds", *Atmospheric Chemistry and Physics*, Vol. 17, No. 11, pp. 6865–6882, 2017.

4. Woźniak, S. B. and D. Stramski, "Modeling the Optical Properties of Mineral Particles Suspended in Seawater and Their Influence on Ocean Reflectance and Chlorophyll Estimation from Remote Sensing Algorithms", *Applied Optics*, Vol. 43, No. 17, pp. 3489–3503, 2004.

5. Hsu, L. C., T. C. Chen, Y. T. Yang, C. Y. Huang, D. W. Shen, Y. T. Chen, and M. C. M. Lee, "Manipulation of Micro-particles through Optical Interference Patterns Generated by Integrated Photonic Devices", *Lab Chip*, Vol. 13, pp. 1151–1155, 2013.

6. Dombrovsky, L. A., J. H. Randrianalisoa, W. Lipinski, and V. Timchenko, "Simplified Approaches to Radiative Transfer Simulations in Laser-Induced Hyperthermia of Superficial Tumors", *Computational Thermal Sciences: An International Journal*, Vol. 5, No. 6, pp. 521–530, 2013.

7. Howell, J. R., M. P. Mengüç, and R. Siegel, *Thermal Radiation Heat Transfer*, Fourth Edition, CRC Press, Boca Raton, 2015.

8. Mishchenko, M. I., "Poynting–Stokes Tensor and Radiative Transfer in Discrete Random Media: the Microphysical Paradigm", *Optics Express*, Vol. 18, No. 19, pp. 19770–19791, 2010.

9. Mie, G., "Beiträge zur Optik Trüber Medien, Speziell Kolloidaler Metallösungen", *Annalen der Physik*, Vol. 330, No. 3, pp. 377–445, 1908.

10. Mishchenko, M. I., ""Independent" and "Dependent" Scattering by Particles in a Multi-Particle Group", *OSA Continuum*, Vol. 1, No. 1, pp. 243–260, Sep 2018.

11. Hottel, H. C., A. F. Sarofim, W. H. Dalzell, and I. A. Vasalos, "Optical Properties of Coatings. Effect of Pigment Concentration", *AIAA Journal*, Vol. 9, No. 10, pp. 1895–1898, 1971.

12. Drolen, B., S. Kumar, and C. Tien, "Experiments on Dependent Scattering of Radiation", *22nd Thermophysics Conference*, pp. 1–8, Honolulu, USA, 1987.

13. Drolen, B. L. and C. L. Tien, "Independent and Dependent Scattering in Packed-Sphere Systems", *Journal of Thermophysics and Heat Transfer*, Vol. 1, No. 1, pp. 63–68, 1987.

14. Yamada, Y., J. D. Cartigny, and C. L. Tien, "Radiatiwe Transfer with Dependent Scattering by Particles: Part 2—Experimental Investigation", *Journal of Heat Transfer*, Vol. 108, No. 3, pp. 614–618, 1986.

15. Howell, J. R. and M. Perlmutter, "Monte Carlo Solution of Thermal Transfer Through Radiant Media Between Gray Walls", *Journal of Heat Transfer*, Vol. 86, No. 1, pp. 116–122, 1964.

16. Mishchenko, M. I., L. D. Travis, and A. A. Lacis, *Multiple Scattering of Light by Particles: Radiative Transfer and Coherent Backscattering*, Cambridge University Press, Cambridge, 2006.

17. Ivezić, Z. and M. P. Mengüç, "An Investigation of Dependent/Independent Scattering Regimes Using a Discrete Dipole Approximation", *International Journal of Heat and Mass Transfer*, Vol. 39, No. 4, pp. 811–822, 1996.

18. Cartigny, J. D., Y. Yamada, and C. L. Tien, "Radiative Transfer with Dependent Scattering by Particles: Part 1—Theoretical Investigation", *Journal of Heat Transfer*, Vol. 108, No. 3, pp. 608–613, 1986.

19. Kaviany, M. and B. Singh, "Radiative Heat Transfer in Porous Media", *Advances in Heat Transfer*, Vol. 23, pp. 133–186, 1993.

20. Quirantes, A., F. Arroyo, and J. Quirantes-Ros, "Multiple Light Scattering by Spherical Particle Systems and Its Dependence on Concentration: a T-Matrix Study", *Journal of Colloid and Interface Science*, Vol. 240, No. 1, pp. 78–82, 2001.

21. Mishchenko, M. I., L. Liu, and G. Videen, "Conditions of Applicability of the Single-Scattering Approximation", *Optics Express*, Vol. 15, No. 12, pp. 7522–7527, 2007.

22. Lee, S. C., "Dependent vs Independent Scattering in Fibrous Composites Containing Parallel Fibers", *Journal of Thermophysics and Heat Transfer*, Vol. 8, No. 4, pp. 641–646, 1994.

23. Galy, T., D. Huang, and L. Pilon, "Revisiting Independent Versus Dependent Scattering Regimes in Suspensions or Aggregates of Spherical Particles", *Journal of Quantitative Spectroscopy and Radiative Transfer*, Vol. 246, p. 106924, 2020.

24. Aoyu, Z., W. Fuqiang, D. Yan, Y. Dongling, and X. Weixin, "Dependent Scattering Criterion Modification of Disordered Dispersed Particulate Medium with the Consideration of Particle Random Distribution and High Complex Refractive Index Effects", *International Journal of Heat and Mass Transfer*, Vol. 197, p. 123331, 2022.

25. Ivezić, Z., M. P. Mengüç, and T. G. Knauer, "A Procedure to Determine the Onset of Soot Agglomeration from Multi-Wavelength Experiments", *Journal of Quantitative Spectroscopy and Radiative Transfer*, Vol. 57, No. 6, pp. 859–865, 1997.

26. Mishchenko, M. I., D. H. Goldstein, J. Chowdhary, and A. Lompado, "Radiative Transfer Theory Verified by Controlled Laboratory Experiments", *Optics Letters*, Vol. 38, No. 18, p. 3522, 2013.

27. Ito, G., M. I. Mishchenko, and T. D. Glotch, "Radiative-Transfer Modeling of Spectra of Planetary Regoliths Using Cluster-Based Dense Packing Modifications", *Journal of Geophysical Research: Planets*, Vol. 123, No. 5, pp. 1203–1220, 2018.

28. Ma, L., J. Tan, J. Zhao, F. Wang, and C. Wang, "Multiple and Dependent Scattering by Densely Packed Discrete Spheres: Comparison of Radiative Transfer and Maxwell Theory", *Journal of Quantitative Spectroscopy and Radiative Transfer*, Vol. 187, pp. 255–266, 2017.

29. Ma, L. X., C. C. Wang, and J. Y. Tan, "Light Scattering by Densely Packed Optically Soft Particle Systems, with Consideration of the Particle Agglomeration and Dependent Scattering", *Applied Optics*, Vol. 58, No. 27, pp. 7336–7345, 2019.

30. Yalçın, R. A., T. Lee, G. N. Kashanchi, J. Markkanen, R. Martinez, S. H. Tolbert, and L. Pilon, "Dependent Scattering in Thick and Concentrated Colloidal Suspensions", *ACS Photonics*, Vol. 9, No. 10, pp. 3318–3332, 2022.

31. Zhai, J., S. Zhang, and L. Liu, "Extinction and Independent Scattering Criterion for Clusters of Spherical Particles Embedded in Absorbing Host Media", *Photonics*, Vol. 10, No. 7, 2023.

32. Väisänen, T., J. Markkanen, A. Penttilä, and K. Muinonen, "Radiative Transfer with Reciprocal Transactions: Numerical Method and Its Implementation", *PLOS*

ONE, Vol. 14, pp. 1–24, 2019.

33. Muinonen, K., J. Markkanen, T. Väisänen, J. Peltoniemi, and A. Penttilä, "Multiple Scattering of Light in Discrete Random Media Using Incoherent Interactions", *Optics Letter*, Vol. 43, No. 4, pp. 683–686, 2018.

34. Planetary System Research, "Incoherent Volume Element Generator (IVEGen)", 2018, https://bitbucket.org/planetarysystemresearch/ivegen_pub, accessed on August 10, 2023.

35. Yalçın, R. A., "Cyaxares", 2023, https://github.com/refetaliyalcin/cyaxares, accessed on July 9, 2023.

36. Yalçın, R. A., E. Blandre, K. Joulain, and J. Drévillon, "Colored Radiative Cooling Coatings with Nanoparticles", *ACS Photonics*, Vol. 7, No. 5, pp. 1312–1322, 2020.

37. Ertürk, H. and J. R. Howell, *Monte Carlo Methods for Radiative Transfer*, Chapter in Monte Carlo Methods for Radiative Transfer, pp. 1–43, Springer International Publishing, Cham, 2017.

38. Durduran, T., R. Choe, W. B. Baker, and A. G. Yodh, "Diffuse Optics for Tissue Monitoring and Tomography", *Reports on Progress in Physics*, Vol. 73, No. 7, 2010.

39. Dombrovsky, L., J. Randrianalisoa, D. Baillis, and L. Pilon, "Use of Mie Theory to Analyze Experimental Data to Identify Infrared Properties of Fused Quartz Containing Bubbles", *Applied Optics*, Vol. 44, No. 33, pp. 7021–7031, 2005.

40. Maruyama, S., "Radiative Heat Transfer in Anisotropic Scattering Media with Specular Boundary Subjected to Collimated Irradiation", *International Journal of Heat and Mass Transfer*, Vol. 41, No. 18, pp. 2847–2856, 1998.

41. Mishchenko, M. I. and P. Yang, "Far-Field Lorenz–Mie Scattering in an Absorb-

ing Host Medium: Theoretical Formalism and FORTRAN Program", *Journal of Quantitative Spectroscopy and Radiative Transfer*, Vol. 205, pp. 241–252, 2018.

42. Videen, G., R. G. Pinnick, D. Ngo, Q. Fu, and P. Chýlek, "Asymmetry Parameter and Aggregate Particles", *Applied Optics*, Vol. 37, No. 6, p. 1104, 1998.

43. Blanchard, C., J.-P. Hugonin, A. Nzie, and D. De Sousa Meneses, "Multipolar Scattering of Subwavelength Interacting Particles: Extraction of Effective Properties Between Transverse and Longitudinal Optical Modes", *Physics Review B*, Vol. 102, p. 064209, Aug 2020.

44. Guinier, A., *X-Ray Diffraction in Crystals, Imperfect Crystals, and Amorphous Bodies*, W. H. Freeman and Company, San Francisco, 1963.

45. Mishchenko, M. I., "Asymmetry Parameters of the Phase Function for Densely Packed Scattering Grains", *Journal of Quantitative Spectroscopy and Radiative Transfer*, Vol. 52, No. 1, pp. 95–110, 1994.

46. Coppens, P., *The Structure Factor*, Chapter in International Tables for Crystallography Volume B: Reciprocal Space, pp. 10–24, Springer Netherlands, Dordrecht, 2001.

47. Ding, K. H., C. E. Mandt, L. Tsang, and J. A. Kong, "Monte Carlo Simulations of Pair Distribution Functions of Dense Discrete Random Media with Multiple Sizes of Particles", *Journal of Electromagnetic Waves and Applications*, Vol. 6, No. 8, pp. 1015–1030, 1992.

48. Aslan, M. M., C. Crofcheck, D. Tao, and M. Pinar Mengüç, "Evaluation of Micro-Bubble Size and Gas Hold-Up in Two-Phase Gas–Liquid Columns via Scattered Light Measurements", *Journal of Quantitative Spectroscopy and Radiative Transfer*, Vol. 101, No. 3, pp. 527–539, 2006.

49. Chae, D., H. Lim, S. So, S. Son, S. Ju, W. Kim, J. Rho, and H. Lee, "Spectrally

Selective Nanoparticle Mixture Coating for Passive Daytime Radiative Cooling", *ACS Applied Materials & Interfaces*, Vol. 13, No. 18, pp. 21119–21126, 2021.

50. Laaksonen, K., S.-Y. Li, S. Puisto, N. Rostedt, T. Ala-Nissila, C. Granqvist, R. Nieminen, and G. Niklasson, "Nanoparticles of TiO2 and VO2 in Dielectric Media: Conditions for Low Optical Scattering, and Comparison Between Effective Medium and Four-Flux Theories", *Solar Energy Materials and Solar Cells*, Vol. 130, pp. 132–137, 2014.

51. Liu, S., X. Wu, Y. Li, S. Cui, X. Shen, and G. Tan, "Hydrophobic In-situ SiO2-TiO2 Composite Aerogel for Heavy Oil Thermal Recovery: Synthesis and High Temperature Performance", *Applied Thermal Engineering*, Vol. 190, p. 116745, 2021.

52. Luk'yanchuk, B. S., N. V. Voshchinnikov, R. Paniagua-Domínguez, and A. I. Kuznetsov, "Optimum Forward Light Scattering by Spherical and Spheroidal Dielectric Nanoparticles with High Refractive Index", *ACS Photonics*, Vol. 2, No. 7, pp. 993–999, 2015.

53. Mackowski, D. W. and M. I. Mishchenko, "A Multiple Sphere T-Matrix Fortran Code for Use on Parallel Computer Clusters", *Journal of Quantitative Spectroscopy and Radiative Transfer*, Vol. 112, No. 13, pp. 2182–2192, 2011.

54. Taufiq, A., R. A. Yalçın, and H. Ertürk, "Evaluation of The Onset of Dependent Scattering in Spherical Particulate Medium Using Superposition T-matrix Method", *Proceedings of the 10th International Symposium on Radiative Transfer*, pp. 251–258, Thessaloniki, Greece, 2023.

55. Bohren, C. F. and D. R. Huffman, *Absorption and Scattering of Light by Small Particles*, John Wiley & Sons, New York, 1983.

56. Hulst, H. V. D., *Light Scattering by Small Particles*, Dover, New York, 1981.

57. Al-Gebory, L., M. P. Mengüç, A. Koşar, and K. Şendur, "Effect of Electrostatic Stabilization on Thermal Radiation Transfer in Nanosuspensions: Photo-Thermal Energy Conversion Applications", *Renewable Energy*, Vol. 119, pp. 625–640, 2018.

58. Al-Gebory, L. and M. P. Mengüç, "A Review of Optical and Radiative Properties of Nanoparticle Suspensions: Effects of Particle Stability, Agglomeration, and Sedimentation", *Journal of Enhanced Heat Transfer*, Vol. 27, No. 3, pp. 207–247, 2020.

59. Barrera, R. G. and A. García-Valenzuela, "Coherent Reflectance in a System of Random Mie Scatterers and Its Relation to the Effective-Medium Approach", *Journal of the Optical Society of America A*, Vol. 20, No. 2, pp. 296–311, 2003.

60. Muinonen, K., J. Markkanen, T. Väisänen, J. I. Peltoniemi, and A. Penttilä, "Multiple Scattering in Discrete Random Media Using First-Order Incoherent Interactions", *Radio Science*, Vol. 52, No. 11, pp. 1419–1431, 2017.

61. Guérin, C. A., P. Mallet, and A. Sentenac, "Effective-Medium Theory for Finite-Size Aggregates", *Journal of Optical Society of America A*, Vol. 23, No. 2, pp. 349–358, 2006.

APPENDIX A: REGIME MAP GRID STUDY

The oscillatory result of the map which is visible especially in the case of monodisperse and at high m can be attributed to the solution of the Lorenz-Mie solution itself. Provided that the grid to build the regime map has enough resolution, the oscillation would present itself. To illustrate the phenomenon, a grid study test was performed. The case was studied based on three different refractive indices, namely, $m = 1.5$, 2.5, and 3.5 for four different grids shown in Figure A.1a, b, c, and d, each represents different grid of 25×25, 50×50, 100×100, and 200×200, respectively. The small dots occupying the map serve as representative of where each the data was captured, and the line represent the value of $E_\sigma = 5\%$. It can be observed that the oscillatory behavior starts as the grid was increased to 100×100 and becomes more pronounced as it is increased to 200×200. The effect was also more visible at high refractive indices such that of m = 2.5 and 3.5.

Grid refinement study must be performed to determine accurate demarcation line. We considered higher resolution grid sets than previously mentioned of 400×400, 1000×200, 200×1000, and 400×1000 shown in Figure A.2a, b, c, and d respectively but this time grid points are not shown for brevity. The similarity of the result given in both grid 200×1000 and 400×1000 suggest that, in the direction of f_v, taking 200 points is sufficient. While in the direction of χ, it is sufficient to have 1000 points, considering grid 400×800 results in similar plot with 200×1000. Since the oscillation is due to Lorenz-Mie solution itself, which is a function of χ and m, it would be logical to prioritize the increase in the number of grid points in the direction of χ only, since f_v does not play a role in the oscillation. Note that the oscillation is much less when polydispersity is included, as shown in Figure A.3. The result of $E_{\sigma'}$ is presented in Figure A.4 to compliment the E_σ data. This study takes 200×1000 for the calculation of the E_σ, E_g, and $E_{\sigma'}$, where only SSF is used. An exception was made for the case of E_R, where radiative transfer equation must be solved. The grid was taken to be 256×256 to lower the computational overhead.

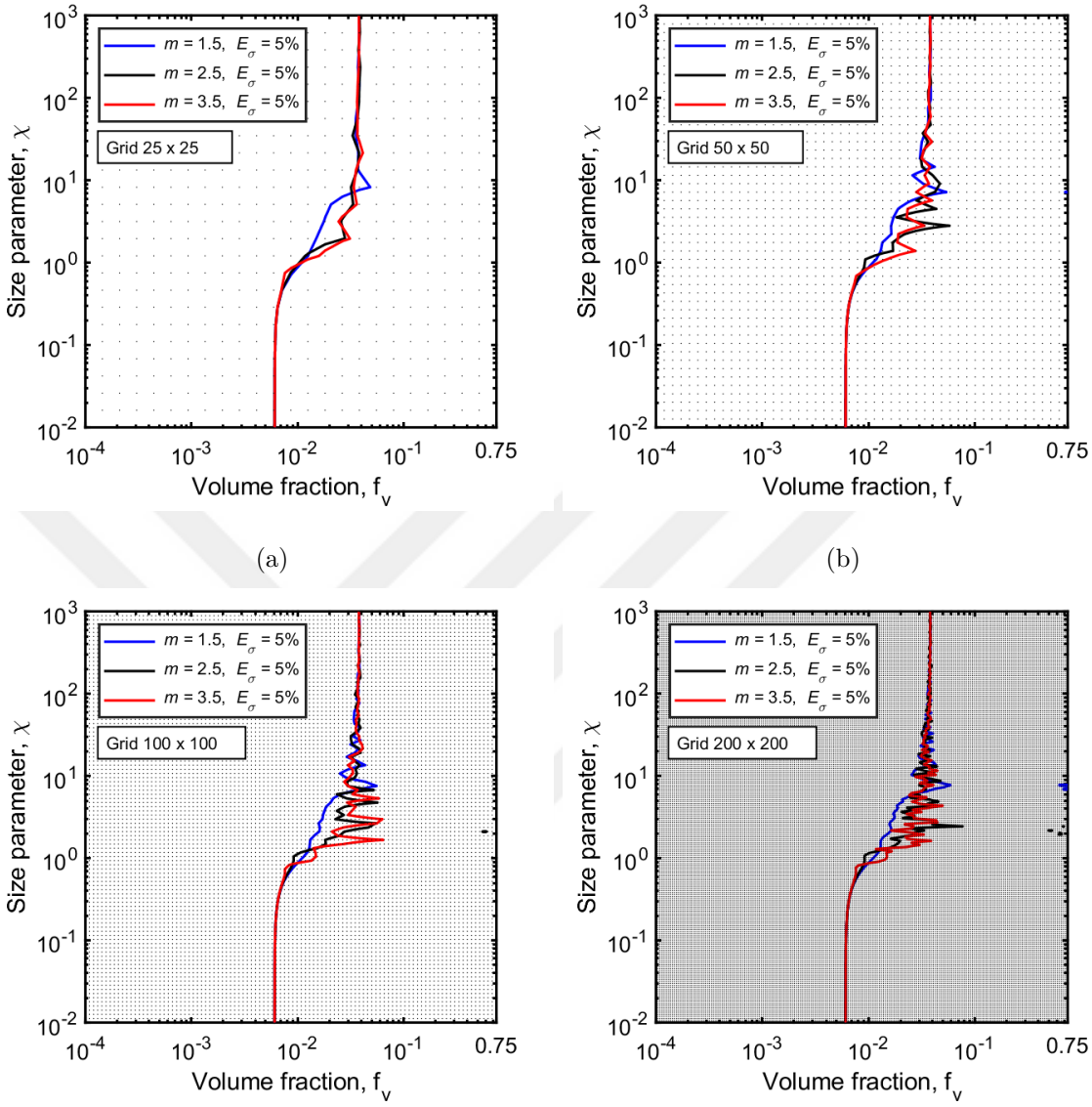

(a) (b)

(c) (d)

Figure A.1. Value of $E_\sigma = 5\%$ for the case of different relative refractive indices ($m = 1.5$, 2.5, and 3.5) with different grid of (a) 25×25, (b) 50×50, (c) 100×100, and (d) 200×200.

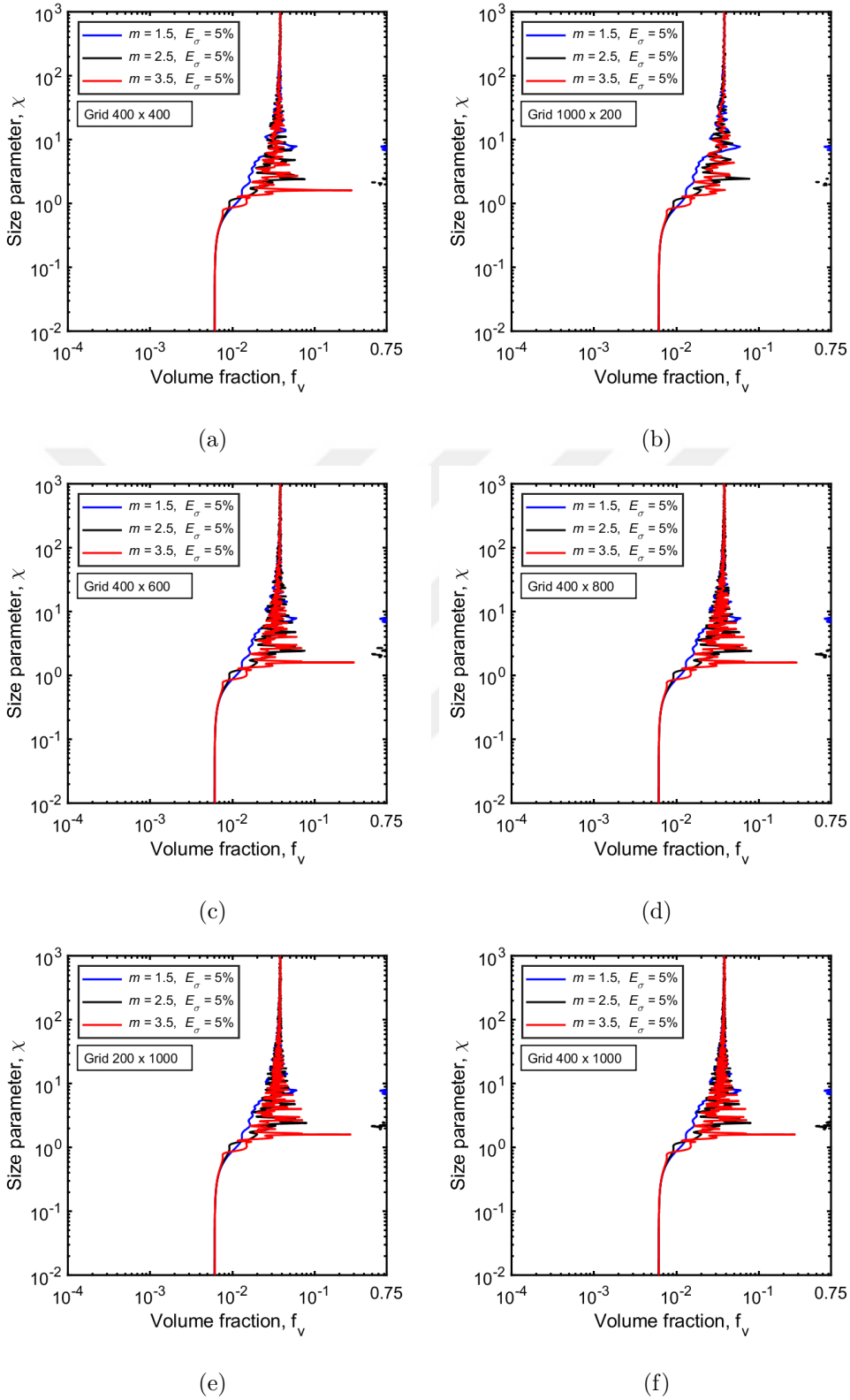

Figure A.2. Value of $E_\sigma = 5\%$ for the case of different relative refractive indices ($m = 1.5$, 2.5, and 3.5), with different grid of (a) 400×400, (b) 1000×200, (c) 400×600, (d) 400×800 (e) 200×1000, and (f) 400×1000.

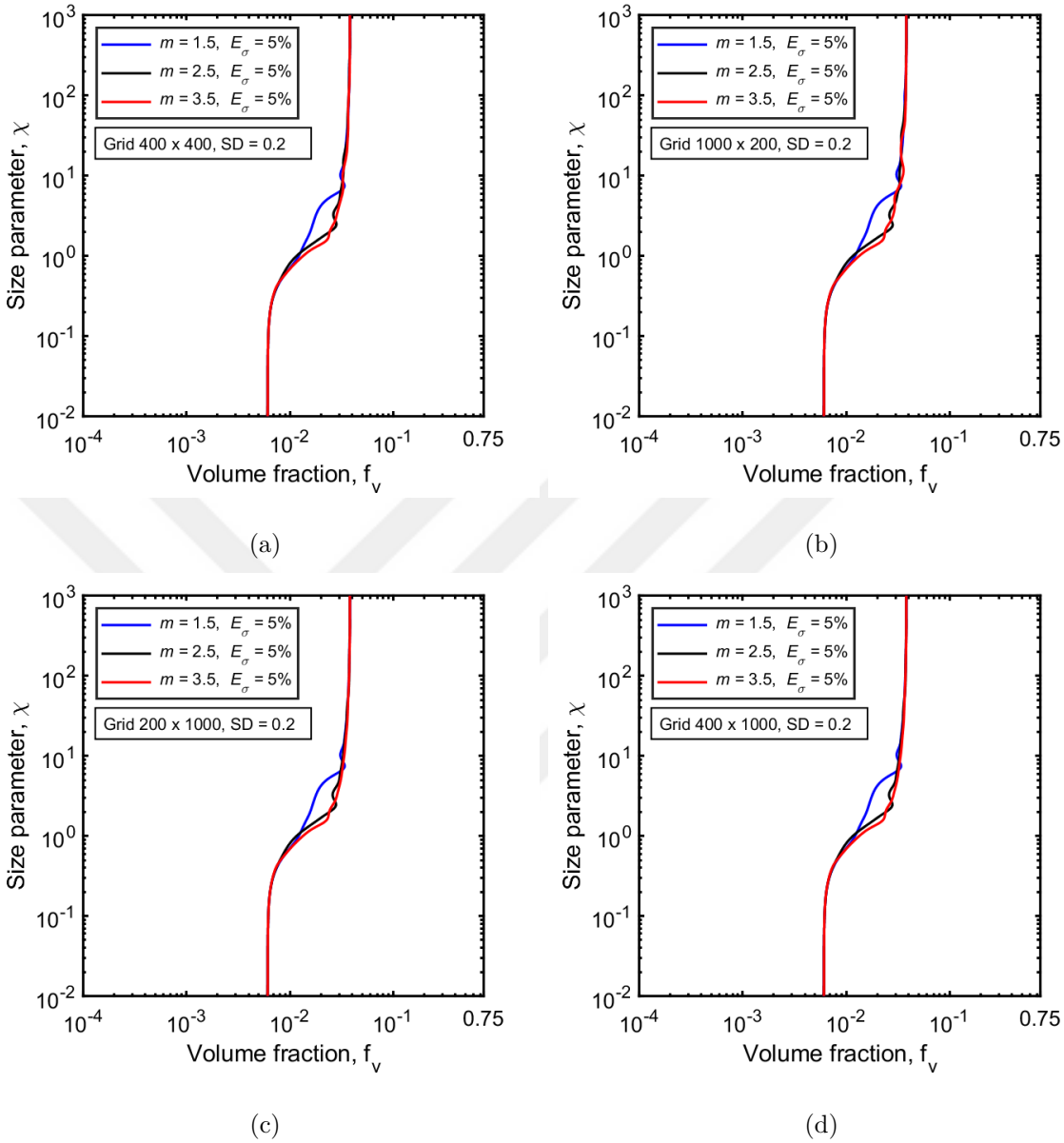

Figure A.3. Value of $E_\sigma = 5\%$ for the case of log-normal polydisperse scatterers, SD = 0.2, for different relative refractive indices ($m = 1.5$, 2.5, and 3.5), with different grid of (a) 400×400, (b) 1000×200, (c) 200×1000, and (d) 400×1000

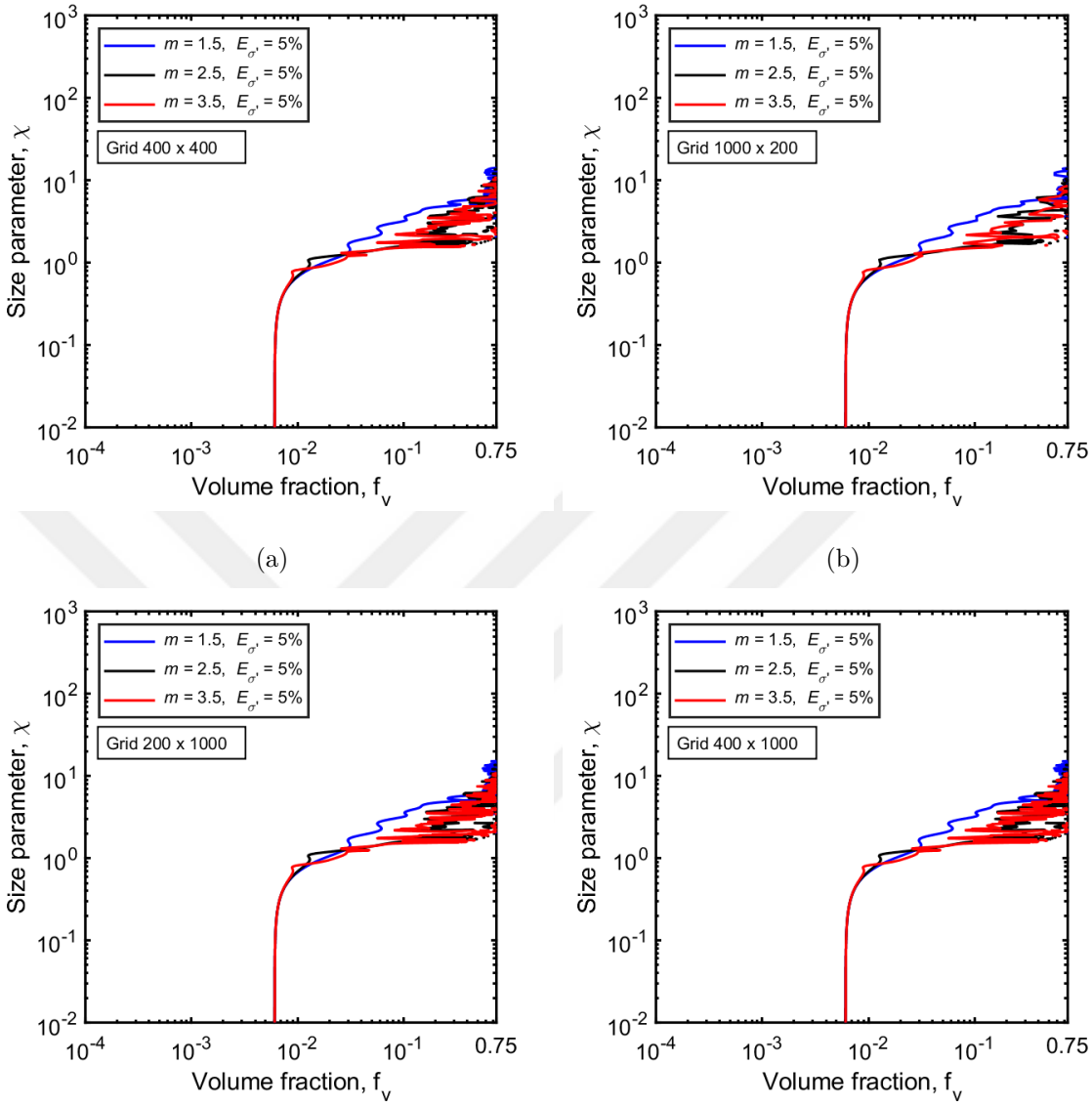

Figure A.4. Value of $E_{\sigma'} = 5\%$ for the case of different relative refractive indices ($m = 1.5$, 2.5, and 3.5), with different grid of (a) 400×400, (b) 1000×200, (c) 200×1000, and (d) 400×1000.

APPENDIX B: SLAB THICKNESS IN MONTE CARLO METHOD

Figure B.1a, b, c, d shows E_R for the case of $m = 1.196$ considering constant thickness ($R_{nh,ind}(L = const.)$). If thickness was to be kept fixed, then the E_R cannot be obtained accurately for some region within the regime map, especially at low f_v and χ. Hence, the result of E_R considering constant thickness would not resemble map produced using $E_{\sigma'}$.

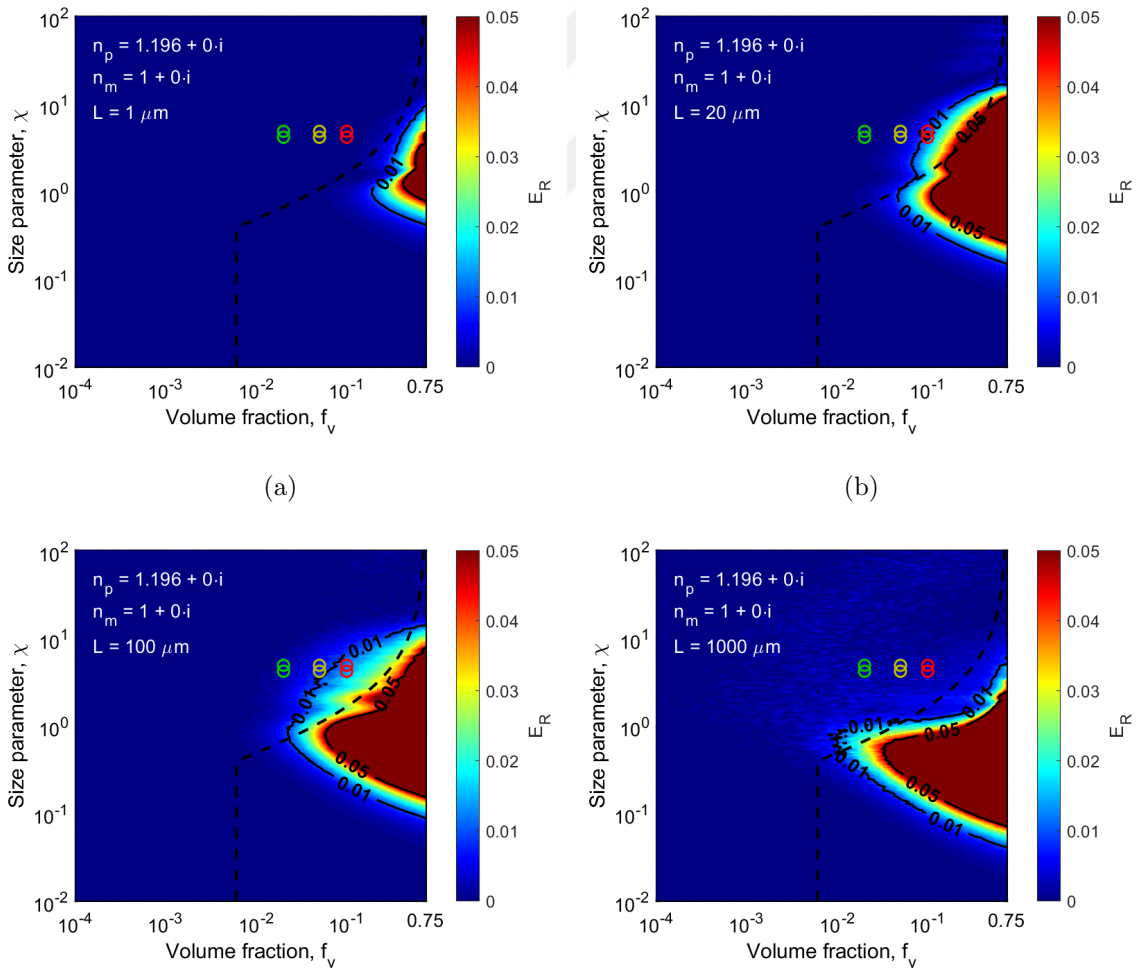

(a) (b)

(c) (d)

Figure B.1. The value of E_R for the case of $m = 1.196$ considering constant thickness, where the value of L is (a) 1 μm, (b) 20 μm, (c) 100 μm, and (d) 1000 μm

To consider constant reflectance regime map, $R_{nh,dep}$, the thickness would need to be varied. Studies were done for the case of $R_{nh,dep} = 0.1$, 0.25, 0.5, and 0.8, and the result is given in Figure B.2a, b, c, d, and e for each $R_{nh,dep}$ values. The thickness varies significantly across the map, with length scale ranging from microscopical 10^{-5} m to a relatively large macroscopical which goes up to 100 km. This result automatically explains why the method relying on constant thickness did not arrive to the same conclusion as the study with constant reflectance and transport scattering coefficient.

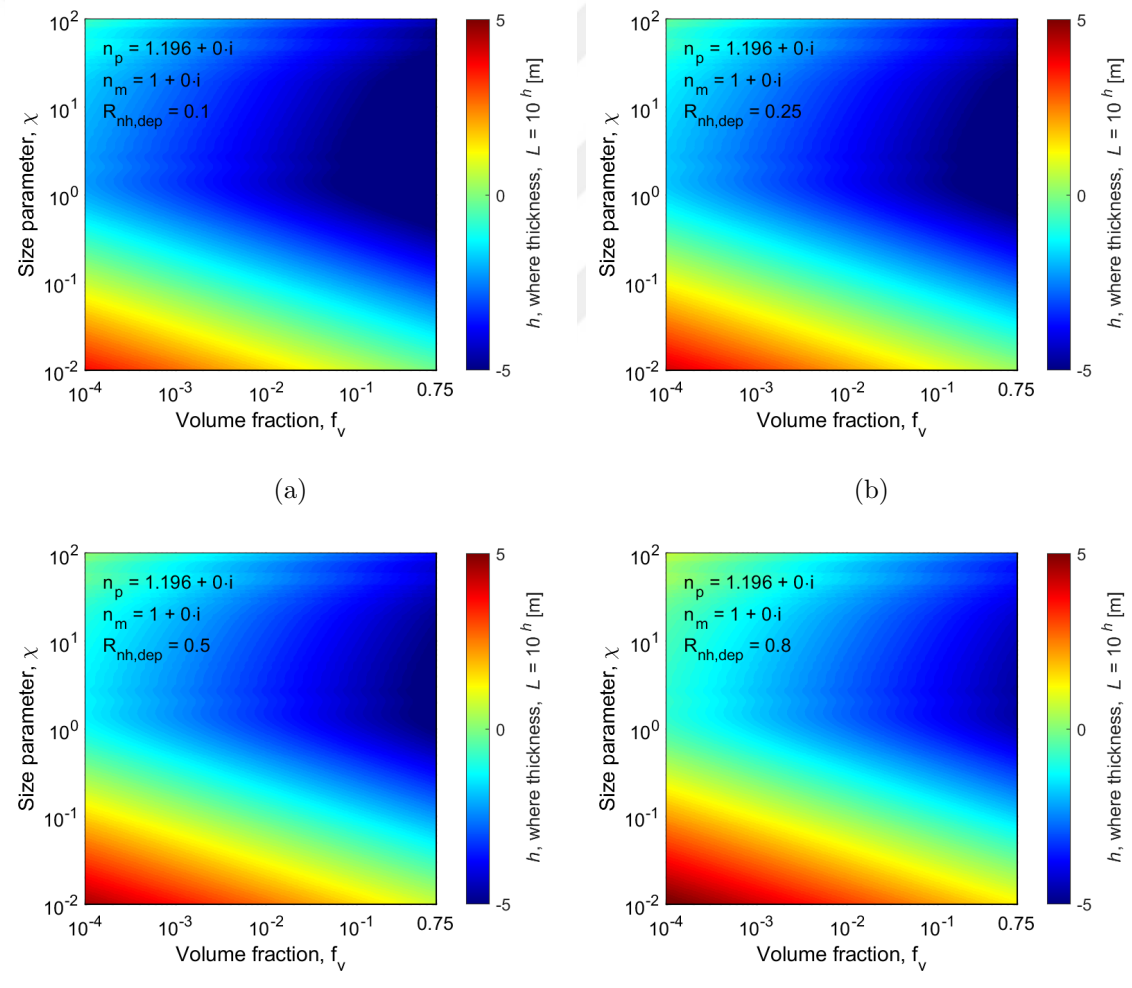

Figure B.2. Value of thickness represented as $L = 10^h$ for the case of different constant $R_{nh,dep}$ value of (a) 0.1, (b) 0.25 (c) 0.5, and (d) 0.8.